The Influence of a Conducting Wall on Disruptions in HBT-EP

Raëd Kombargi

Submitted in partial fulfillment of the

requirements for the degree

of Doctor of Philosophy

in the Graduate School of Arts and Sciences

COLUMBIA UNIVERSITY

1997

Table of Contents

4

List of figures and tables

Chapter 5 DIAGNOSTICS AND OPERATION

Chapter 6 WALL STABILIZATION STUDIES

9

Chapter 1
INTRODUCTION

The definition of energy according to the Webster's dictionary [1] is as follows:

Energy: 1. the capacity for vigorous activity; 2. the ability of matter or radiation to do work either because of its motion (kinetic energy), or because of its mass (released in nuclear fission etc.), or because of its electric charge etc.; 3. fuel and other resources used for the operation of machinery etc.

Human civilization and its progress depend on energy. A combination of a growing world population (currently ˜ 4.7 billion people) and expanding energy needs will exhaust oil and natural gases in the next century. Scientists and engineers, foreseeing future problems of increased energy consumption and dwindling supplies, are searching for new sources of power (solar, windmills etc.).

1.1 Atomic energy

In 1905, Einstein, the last of the great classical physicists, not only revolutionized the way people perceive the notions of time and space with his theory of relativity, he also laid the theoretical foundations of atomic energy with his famous equivalence of mass and energy summarized in the now commonly known equation $E = (\Delta m)c^2$. The idea is that atomic energy can be generated from a change in mass of the *nucleus*, the inner high density core of an atom, where most of the mass is concentrated.

Nuclei consist of protons $(1.673 \times 10^{-27} Kg, \ +1.6 \times 10^{-19} C)$, neutrons $(1.675 \times 10^{-27} Kg, \ 0 \ C)$ and revolving electrons $(9.1098 \times 10^{-31} Kg, \ -1.6 \times 10^{-19} C)$. A strong *attractive* force called the *nuclear* force binds protons and neutrons together in a nucleus and

acts on nuclei that are separated by less than $5 \times 10^{-15} m$. A *repulsive* force, called the *Coulomb* force acts on particles (e.g. protons, electrons) with the same kind of charge. Energy release from "nuclear" processes like fission and fusion is the result of the combined effects of the coulomb force between protons and the nuclear force between *nucleons* (neutrons or protons). In the case of nuclear fission, when a fissionable nucleus captures a neutron, the internal force balance between the nucleons of the nucleus is disturbed. Repulsion between protons within the nucleus becomes stronger than the required attractive force that holds the nucleons together, the nucleus turns unstable and usually splits into lighter nuclei and two or three neutrons. As an example, Uranium (amu=235) may, upon absorption of a neutron, fission into Cesium (amu=140), Rubidium (amu=93) and three neutrons. Some mass disappears during the process and this mass defect is manifested as an energy release. For nuclear fusion the mechanism is reversed. Two very light atoms such as the two Hydrogen isotopes, Deuterium (amu=2) and Tritium (amu=3), can be fused, once the electrostatic repulsion between the protons is overcome, to produce the much more tightly bound Helium atom (amu=4) giving off considerable energy resulting from the mass defect occurring in the process [2].

1.2 Historical overview

With these concepts in mind, Bethe published a paper in the 1930's explaining that the origin of energy radiated from the sun and other stars is a series of exoergic nuclear reactions [3]. Around that time, Rutherford also produced laboratory fusion reactions from deuteron beam collisions [4]. It was not until W.W.II that these ideas were dramatically validated with the successful detonation of nuclear fission bombs (1940's) and later fusion "hydrogen" bombs (1952 in the Marshall Islands). The challenge was to develop nuclear fusion and fission as

2

controlled energy sources for the advancement of mankind and not its annihilation. Although originating from the same conception and at about the same time, controlled fission energy and controlled fusion energy progressed at different paces. While fission based power plants are on line producing electricity in Europe, Japan and the USA, fusion based power plants are only designs on paper, awaiting more advanced scientific methods.

1.3 Tokamaks

Nuclear-fusion energy has significant advantages over nuclear-fission energy: a virtually unlimited supply of fuel, greatly reduced amount of radioactive waste and the possibility of generating electric energy more directly than through conventional heat exchangers and turbines. However, formidable difficulties remain a barrier to the achievement of power sources based on controlled nuclear fusion. In order to " fuse", fuel atoms, brought close enough to one another so as to collide, must be at sufficiently high temperatures, on the order of 10^8 °K (10 KeV), to overcome the Coulomb repulsion between the interacting nuclei. At these temperature levels, the constituent atoms of the fuel gas become *ionized*, meaning all electrons have been removed from them. Such a collection of electrically charged particles, free electrons and bare nuclei, is called a *plasma* . Hot plasmas must be enclosed long enough so that "fusion" reactions can take place between the plasma particles. Ordinary containers are not suitable as they could either melt from the very hot plasma or else cool the plasma below the temperature of spontaneous nuclear fusion. One technique of isolating a hot plasma from its surroundings is the method of *magnetic confinement* . The plasma is prevented from striking the walls of its container by means of magnetic fields, similar to the way that charged particles are trapped within the Earth's Van Allen belts by the Earth's magnetic field.

3

One of the earliest magnetic confinement experiments was carried out by Bennett [5] in his pinch-effect experiment. This linear pinch approach suffers from significant energy losses at the ends of the column. A *closed* magnetic configuration was used to eliminate these end losses and scientists have focused most recent efforts on toroidal devices. The most successful to date of these closed magnetic bottles is the *tokamak* [6,7]. The name is a Russian acronym, it consists of the first syllables of the Russian words: "toroid", "kamera" (chamber), "magnit" (magnet), plus the first letter of the word "katushka" (coil). Fig 1.1 shows a schematic of the essential components of a tokamak as well as plasma geometry.
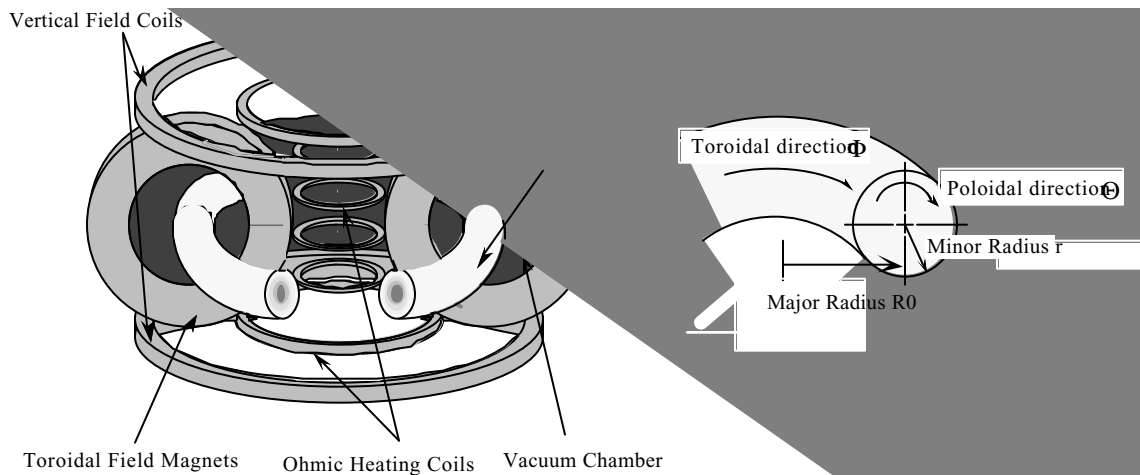
Fig 1.1 Schematic of a tokamak

A strong toroidal magnetic field is generated by the toroidal field system, creating a closed magnetic configuration necessary but not sufficient for proper confinement. Particle vertical drifts occur because the toroidal field is stronger on the inboard side of the tokamak since the field lines are bent. Inserted into this coil system a toroidal vacuum chamber is filled with Hydrogen or its isotopes under low pressure. This gas together with the ohmic heating coils form a transformer system with the primary windings being the ohmic heating coils and the gas

acting as the secondary. When current is driven through the primary winding, an inductive electric field is produced inside and directed along the chamber. When this field is high enough, a gaseous break-down occurs, a closed plasma ring is formed and a so-called *plasma current* starts flowing toroidally within it. The current heats the plasma to high temperatures and generates a poloidal magnetic field that encloses it. The sum of this field and the toroidal field creates helical field lines that confine the plasma and its particles, eliminating the charge separation caused by the vertical magnetic drift. Finally, a vertical magnetic is applied that interacts with the current in the plasma creating a force that counters the outward expansion of the plasma in the major radius direction. This expansion comes from two forces: one is caused by the kinetic pressure of the plasma due to the curvature of the system and the other results from the interaction of the toroidal plasma current and the poloidal field; this latter force is also known as the hoop force. A detailed description of tokamaks and a good review of several tokamak plasmas issues are presented in a recent book by Kadomtsev [8].

Large tokamaks with additional heating sources were developed throughout the 1970's and 1980's and equipped with advanced diagnostic systems for plasma parameters measurements. The initial physical concept of a tokamak was simple: a plasma ring with a toroidal current immersed in a strong magnetic confining configuration. However, plasma instabilities and tokamak disruptions have slowed down the development of controlled thermonuclear fusion using tokamak devices. The investigation of the most dangerous disruptive instabilities is the subject of this thesis.

1.4 Disruptions in tokamaks

Tokamak disruptions are dramatic events that abruptly terminate the plasma discharge and cause a loss of plasma and particle confinement. Disruptions are called minor if they alter the plasma confinement for a brief duration in the discharge's lifetime without causing a complete collapse and loss of the plasma current channel. Disruptions are called major if they lead to nearly total loss of both current and confinement. Disruptions occur and are observed routinely on all tokamaks. They are a serious concern for future tokamaks reactors. For example electromagnetic forces associated with current and energy quenches can give rise to large mechanical stresses that can destroy the mechanical structure of large machines. Also, rapid energy losses may result in damaging heat and particle fluxes to the nearby walls of the vacuum chamber. For present-day research tokamaks, disruptions limit allowed operating parameters.

1.4.1 Tokamak operational parameters

The operation of a tokamak is characterized by its current , density and pressure. These can be expressed in terms of the three dimensionless parameters.

a) <u>The safety factor, q</u>

It is a measure of the pitch of the helical magnetic field lines. It is defined as the number of times that a magnetic field line must traverse the torus toroidally to exactly wrap once around the poloidal cross section. It has the form

$$q = \frac{1}{2\pi} \oint \frac{B_\Phi}{R B_P} dl_P \qquad (1.1)$$

where R is the plasma major radius, B_Φ the toroidal field, B_P the poloidal magnetic field and the line integral corresponds to one poloidal circuit. A related quantity, more easily measured, is

the equivalent boundary safety factor, q^*. This is also known as the *"cylindrical q"* and is defined as follows

$$q^* \equiv \frac{a\mathrm{B}_{\Phi 0}}{R\bar{\mathrm{B}}_\mathrm{P}} \qquad (1.2)$$

where a is the plasma minor radius, $\mathrm{B}_{\Phi 0}$ the toroidal field at R and $\bar{\mathrm{B}}_\mathrm{P}$ the poloidal magnetic field averaged over the plasma boundary. Calculating $\bar{\mathrm{B}}_\mathrm{P}$ for a circular cross section plasma and substituting in Eq. (1.2), q^* becomes

$$q^* = \frac{2\pi a^2 \mathrm{B}_{\Phi 0}}{\mu_0 R \mathrm{I}_\mathrm{P}} \qquad (1.3)$$

where I_P is the total plasma current in the toroidal direction and $\mu_0 = 4\pi \times 10^{-7}$. The MKS system of units is used throughout this thesis.

b) The normalized line averaged electron density

The quantity commonly used to describe densities in tokamaks is $\bar{n}_e \dfrac{R}{\mathrm{B}_{\Phi 0}}$ where $\bar{n}_e$ is the line averaged electron density and the standardization is to the size of the tokamak as characterized by its toroidal magnetic field and its major radius. When normalized to $1 \times 10^{19} m^{-2} \cdot \mathrm{T}^{-1}$, this becomes the dimensionless Murakami number [9]. This number is unity at the historical density limit of tokamaks.

c) The volume averaged plasma beta

The quantity β is an important dimensionless parameter. It is defined as the ratio of the plasma pressure to the magnetic field pressure. It is a measure of the efficiency of the confining magnetic field in enclosing the plasma. The average toroidal beta has the form

$$\beta \equiv \frac{2\mu_0 \langle \mathrm{P} \rangle}{\mathrm{B}_{\Phi 0}^2} \qquad (1.4)$$

7

where $\langle P \rangle$ is the volume averaged pressure of the plasma and $B_{\Phi 0}$ is the vacuum toroidal field at the major radius (also written B_T). Likewise, the average poloidal beta is defined as

$$\beta_P \equiv \frac{2\mu_0 \langle P \rangle}{\bar{B}_P^2} \qquad (1.5)$$

where $\bar{B}_P$ is the poloidal magnetic field averaged over the plasma boundary. A high value of beta is advantageous since fusion power density can be shown to be proportional to β^2.

1.4.2 Tokamak operational domain

a) Current and density limits

Tokamaks disrupt when the density or current exceed certain values. The restricted operational range in the current and density domain parameter space can be represented by the so-called Hugill diagram [10] where the Murakami parameter [9] $n_e \frac{R}{B_T}$ is plotted vs. 1/q. The current limit is given by q > 2 and the density limit, which is proportional to the average current density, by $\frac{\bar{n}_e R}{B} \approx \left(2/q_{cyl}\right) \times 10^{20} \left(m^{-2}.T^{-1}\right)$.

b) Beta limit

It is an experimental fact, supported by strong theoretical evidence, that there is a limit to the beta value that can be achieved. As plasma pressure increases through auxiliary heating sources such as neutral beams or radio frequency heating, an operational β-limit is observed. It manifests itself either as a hard disruption or as a soft limit with strong confinement degradation saturating the pressure. Troyon and Sykes [11,12] first suggested that this limit is due to the onset of instabilities predicted by the *ideal magnetohydrodynamic* (MHD) plasma model. MHD instabilities are characterized by a toroidal mode number n and a poloidal mode number

8

m. The most dangerous of these instabilities are the low-n *external* modes, where external refers to the fact that the resonant surface of the instability is outside the plasma boundary (internal modes have resonant surfaces inside the plasma). Particularly volatile is the n=1 *external kink* mode which is a helical distortion of the outer boundary of the plasma. It can be a current driven or a pressure driven instability. Operationally, the threshold for β-limiting instabilities is now the widely accepted Troyon β-limit [11] of $\beta_{max} \propto \dfrac{I_P}{a B_\Phi}$. This is also expressed as a stability boundary through the Troyon-normalized beta defined as follows:

$$\beta_N \equiv \beta(\%)\frac{a(m)B_\Phi(T)}{I_P(MA)} = \beta(\%)\frac{\mu_0(R/a)q^*}{2\pi} \times 10^6 \tag{1.6}$$

The beta limit of a tokamak is related to its magnetic geometry $\propto a/Rq^*$. Typically, the onset of the n=1 external kink instability occurs when β_N reaches values near 3.

1.5 HBT-EP

The HBT-EP (High Beta Tokamak - Extended Pulse) device is the third tokamak experiment built at Columbia University. The plasma parameters of HBT-EP are chosen so that an extrapolation of the results to larger tokamaks is possible. The design goals are an electron temperature $T_{e0} \approx 100 eV$, a magnetic Reynolds number $S \approx 10^4 - 10^5$ and a plasma β near the Troyon β-limit using ohmic heating only.

The magnetic Reynolds number (or Lundquist number) is defined as follows:

$$S \equiv \frac{\tau_R}{\tau_A} \tag{1.7}$$

Here τ_R is the characteristic time for resistive diffusion of fields through the plasma. It is calculated as follows:

$$\tau_R = \mu_0 \frac{a^2}{\eta} \tag{1.8}$$

where a is the plasma minor radius and η is the plasma resistivity. τ_A is the poloidal transit time of a shear Alfvén wave. It is the typical time scale of the growth of ideal MHD modes. τ_A is given by $\tau_A = \sqrt{\mu_0 \rho} \frac{a}{\bar{B}_P}$ where ρ is the plasma mass density and $\bar{B}_P$ is the average value of the poloidal magnetic field. The typical time scale of the growth of resistive MHD modes, τ_η, can be shown to be an expression $\propto S^{3/5} \tau_A$ [13]. Therefore a large magnetic Reynolds number means a significant distinction between the growth time of ideal and resistive MHD modes. A ratio of $\tau_\eta / \tau_A \approx 10^4$ is adequate to distinguish resistive and ideal effects.

The other design objective is that of increased temperature. The plasma should be hot enough to have fully ionized all impurity atoms, in particular oxygen which has a large cross section for collisional excitation [14,15]. The temperature at which the radiative barrier due to oxygen is surpassed is usually a function of time and plasma density. For coronal equilibrium [16], this barrier temperature can be calculated and is $\approx 20 - 40 eV$.

The use of ohmic heating only to obtain high-β discharges is advantageous since other external power sources such as neutral beams or non-ohmic heating systems are technically demanding and expensive. The previous Columbia device, HBT [17], used ohmic heating only to reach the β-limit by operation with plasma densities at or above the conventional density limits. HBT-EP makes use of a fast ohmic heating system capable of rapid discharge startup and

sustained high loop voltage. Table I.1 below shows parameters obtained in HBT-EP and other existing devices.

	HBT	HBT-EP	JET	TFTR	DIII-D	PBX-M
Major Radius R0 (m)	0.24	0.92	3.0	2.48	1.67	1.4
Minor Radius a (m)	0.07	0.15	1.25	0.85	0.62	0.44
Plasma Current Ip (kA)	10	25	5000	3000	3000	600
Electron Temperature Te (keV)	0.03	0.1	12	12	2	2.2
Electron Density $n_e \left(\times 10^{19} m^{-3} \right)$	3-6	1	4	1	3	4-8
Toroidal Magnetic Field $B_{\Phi 0}$ (T)	0.3	0.35	3.2	5.2	2.6	1.1
Pulse Length τ_P (s)	< 0.002	< 0.012	> 10	> 7	> 10	> 1.0

Table I.1 Plasma parameters comparison for several tokamaks

The physics goals of HBT-EP are:

1. Achieve high beta performance using ohmic heating only in a relatively modest size, reasonably well diagnosed machine [18]. This goal allows the study of β-limiting external kink instabilities.

2. Demonstrate passive stabilization of β-limiting, rapidly growing disruptive MHD instabilities using a set of movable, close-fitting conductors placed in the vacuum chamber. Initial results showed that discharges reach higher values of beta without disruption when the conducting walls are moved close to the surface of the plasma [19,20].

3. Demonstrate active control of remaining slower growing modes using external saddle coils and power amplifiers. The magnetic fields from the saddle coils provide the means to investigate both asynchronous and synchronous feedback. Initial results show acceleration or deceleration of the frequency of slowly growing modes and mode amplitude reduction during brief intervals of phase synchronism [20].

11

The n=1 external kink mode, seen in HBT-EP in conjunction with β-limiting disruption and with slowly ramped discharges, can be stabilized either by the use of a nearby conducting wall surrounding the plasma or the control and/or modification of plasma profiles. Both profile control and plasma-wall separation adjustments will probably be required to eliminate disruptive instabilities. In HBT-EP, profiles are changed transiently using current ramps. Plasma-wall separation is modified between discharges by adjusting the position of a conducting wall around the plasma. The presence of the movable conducting plates inside the vacuum chamber and the variety of available diagnostics on HBT-EP makes a detailed study of the effects of these conducting walls on mode stabilization possible.

1.6 Principal results

Two types of discharges were selected to study the influence of a conducting wall on disruptions in HBT-EP. One category of plasmas was used to test the effects of the conducting wall on current-driven external kinks and the other category was used to examine the wall effects on β-limiting disruptions.

- Results from conducting wall experiments demonstrate that fast-growing, low-n kink instabilities were suppressed if the conducting wall sections were positioned sufficiently near the plasma (b/a < 1.2 where b is the radial position of a conducting wall segment and a is the minor radius of the plasma) and a slight positive current ramp ($dI_P/dt > 0$) was maintained.

- Wall stabilization of disruption precursor modes was observed both in plasmas with strong current ramps and in discharges near the Troyon limit.

12

- As the current profile evolved $(dI_P/dt < 0)$, wall-stabilized discharges eventually disrupted because of internal modes.

- The disruption of plasmas with b/a=1.52 was due to external events as opposed to the disruption of plasmas with b/a=1.07 which was due to internally induced mechanisms. The external disruption were eliminated when the conducting wall was moved from b/a=1.52 to b/a=1.07. The internal disruption could not be avoided even with b/a=1.07.

1.7 Outline of the thesis

Chapters 2 is a review of the MHD theory, both equilibrium and stability are explained. Chapter 3 is a disruption review where a summary of the present understanding of that phenomena is given. Chapters 4 and 5 describes HBT-EP and its diagnostics in details. Chapter 6 contains the analysis and principal results of this work and chapter 7 is a summary and discussion.

References

 [1] Webster's New Universal Unabridged Dictionary, 2nd edition, (New world Dictionaries, Simon & Schuster, 1972).

[2] D. Bodansky, *Nuclear Energy*, (AIP press, Woodbury, NY 1996).

[3] H.A. Beth, Phys. Rev. **55** 434 (1939).

[4] E. Rutherford, Science **80** 221 (1934).

[5] W.H. Bennett, Phys. Rev. **45** 890 (1934).

[6] A.D. Sakharov and I.E. Tamm, *Plasma Physics and the Problem of Controlled Thermonuclear Reactors,* (Pergamon, NY 1959-1960), Vol 1 first three articles.

[7] L.A. Artismovich, Nuc. Fusion **12** 215 (1972).

[8] B. Kadomtsev, *Tokamak Plasma: A Complex Physical System* (Plasma Physics Series, Institute of Physics Publishing, Bristol & Philadelphia, 1992).

[9] M. Murakami et al., Nuc. Fusion **16** 347 (1976).

[10] K.B. Axon et al., Plasma Physics and Controlled Nuclear Fusion Research **1980** IAEA, Brussels (1980).

[11] F. Troyon et al., Plasma Physics and Controlled Fusion **26** 209 (1984).

[12] A. Sykes et al., Controlled Fusion and Plasma Physics (European Physical Society, Aachen, 1983).

[13] G. Bateman, *MHD Instabilities*, (MIT press, Cambridge, 1978).

[14] R.C. Isler, Nuc. Fusion **24** 1599 (1984).

[15] D. Post et al., Atomic Data and Nuclear Tables **20** 397 (1977).

[16] H. Griem, *Plasma Spectroscopy*, (McGraw-Hill, NY 1964).

[17] G.A. Navratil et al., Plasma Physics and Controlled Nuclear Fusion Research **1986** IAEA, Kyoto (1986).

[18] M.K.V. Sankar et al., J. Fusion Energy **12** 303 (1993).

[19] D. Gates, Ph.D. thesis, Columbia University, 1993.

[20] T.H. Ivers et al., Plasma Physics and Controlled Nuclear Fusion Research **1994** IAEA, Seville (1994).

14

Chapter 2
MAGNETOHYDRODYNAMICS

2.1 Plasmas as fluids

The plasma state refers to high temperature matter consisting of free electrons and ions exhibiting collective behavior. Where as gas particles undergo binary collisions that control their motion, plasma particles are charged and as a result are subject to long range electromagnetic forces. The unique physics of plasma comes from the fact that the statistical properties of plasmas are a result of the long-range Coulomb interactions and involve many particles interacting simultaneously.

How are plasmas described? How is plasma dynamics computed? One answer is to think of plasmas as a collection of particles and follow the separate motion of each individual one. The equations of motion for each charged particle must be solved subject to externally prescribed forces (e.g. applied electromagnetic fields, gravitational fields) and internally generated magnetic or electric fields determined by the positions and motions of the charges. This must be done dynamically and in a manner consistent with Maxwell's equations. For large plasma devices, like tokamaks, with particle densities of $10^{19} - 10^{20}$ per m^3, this direct method is impossible even with the world's fastest super computers.

A more practical approach is to follow the evolution of the statistical properties of a plasma, rather than solving for each individual particle. A kinetic classification of the plasma can be adopted. The kinetic theory of plasmas describes the behavior of the distribution function, $f(\vec{x}, \vec{v}, t)$, which measures the probability density of a single particle in a six-dimensional phase space $(\vec{x}, \vec{v})$. This type of modeling is successful in explaining some

microscopic plasma behavior such as collision dynamics, micro-instabilities and wave particle resonance. Although, a great simplification, the kinetic approach is still too difficult to solve in any non-trivial geometry for long time scales.

Fortunately, the majority of plasma phenomena observed in real experiments, such as equilibrium and stability properties in tokamaks, can be explained using a fluid description of a plasma. This model results from taking velocity moments of the kinetic equations; only the dynamics of the low-order moments, like density, flow and pressure is taken into account. The model works well for tokamak plasmas and is used frequently in transport and stability calculations.

2.2 The MHD equations

The magnetohydrodynamic (MHD) description of plasmas and their macroscopic properties is one of the more simple and most successful models in predicting tokamak phenomena and plasma behavior in it. The MHD equations can be derived by combining the fluid descriptions of each plasma species (e.g. electrons and ions) to form equations for the mass density, mass flow, pressure and plasma current. A detailed derivation and explanation of ideal MHD theory can be found in textbooks [1,2]. The MHD equations for a plasma are:

$$\frac{\partial \rho}{\partial t} + \nabla \cdot \rho \vec{v} = 0 \tag{2.1}$$

$$\rho \frac{d\vec{v}}{dt} = \vec{J} \times \vec{B} - \nabla p \tag{2.2}$$

$$\vec{E} + \vec{v} \times \vec{B} = \eta \vec{J} \tag{2.3}$$

$$\frac{d}{dt}\left(\frac{p}{\rho^{\gamma}}\right) = 0 \tag{2.4}$$

$$\nabla \times \vec{E} = -\frac{\partial \vec{B}}{\partial t} \tag{2.5}$$

$$\nabla \times \vec{B} = \mu_0 \vec{J} \tag{2.6}$$

$$\nabla \cdot \vec{B} = 0 \tag{2.7}$$

Here the electromagnetic variables are the magnetic field $\vec{B}$, the electric field $\vec{E}$ and the current density $\vec{J}$. The fluid variables are the mass density ρ, the fluid velocity $\vec{v}$ and the pressure p. Also, η is the plasma resistivity, γ the ratio of the specific heats and $d/dt = \partial/\partial t + \vec{v} \cdot \nabla$ is the convective derivative. Equations (2.1), (2.2) and (2.4) represent the time evolution of mass, momentum and energy, respectively. Generally, γ is taken to be 5/3. Equation (2.3), Ohm's law, relates the current density to the field quantities evaluated in the laboratory frame of reference. If the plasma resistivity η is taken to be zero, implying that the plasma has an infinite conductivity, Eqs. (2.1)-(2.7) are called the *ideal MHD* equations. This ideal assumption has the effect that the magnetic field lines are forced to move with the plasma, they are *frozen in* and the field line topology must be preserved during any allowable MHD motion. Equations (2.5)-(2.7) are just the low frequency magnetostatic equations.

The conditions of validity of the ideal MHD equations are, as per Friedberg [1], small gyro radius (Larmor radius) compared to the characteristic length scale of the system, usually the minor radius a ; high collisionality meaning a short plasma particle mean free path as compared to the typical dimensions of the system; and finally, the requirement of small resistivity or low η, making the $\eta \vec{J}$ term in Ohm's law negligible compared to $\vec{v} \times \vec{B}$. This means that the time scale of plasma diffusion across the magnetic field lines is longer than other MHD time scales of interest. These three conditions can be expressed as

(small gyro radius) $\quad\quad\quad\quad r_{Li} << a$ $\quad\quad\quad\quad\quad\quad\quad$ (2.8.1)

17

(short mean free path) $v_{Ti}\tau_{ii} << a$ (2.8.2)

(small resistivity) $\dfrac{(m_e/m_i)^{1/2}}{(v_{Ti}/a)\tau_{ii}}\left(\dfrac{r_{Li}}{a}\right)^2 << 1$ (2.8.3)

Here m_e, m_i are the electron and ion masses, v_{Ti} is the ion thermal velocity, a is the plasma minor radius, τ_{ii} is the ion-ion collision time and r_{Li} is the plasma ion gyro radius.

Numerical values for the MHD validity conditions can be calculated for a typical HBT-EP discharge. The plasma parameters used are $T_e = T_i = 50 eV$, $n_e = n_i = 10^{19} m^{-3}$, a=0.15 m and $B_{\Phi 0} = 0.35$ T. The calculations yield the following results

$$r_{Li} \approx 0.003m << a = 0.15m$$

$$v_{Ti}\tau_{ii} \approx 34.3 \times 10^{-5} m << a = 0.15m$$

$$\frac{(m_e/m_i)^{1/2}}{(v_{Ti}/a)\tau_{ii}}\left(\frac{r_{Li}}{a}\right)^2 \approx 4 \times 10^{-3} << 1$$

verifying that the ideal MHD equations are indeed valid for HBT-EP plasmas.

2.3 MHD equilibrium

When a system reaches equilibrium it means that its dynamically varying quantities are no longer changing with time. In the case of the ideal MHD model, considering steady state without flow ($\vec{v} = 0$) translates into the following:

$$\nabla p = \vec{J} \times \vec{B} \tag{2.9}$$

$$\nabla \times \vec{B} = \mu_0 \vec{J} \tag{2.10}$$

$$\nabla \cdot \vec{B} = 0 \tag{2.11}$$

18

Equation (2.9) is the expression of a force balance given by the time-independent portion of the momentum equation. Equations (2.10) and (2.11) are the relevant Maxwell's equations. Taking the inner products of $\vec{B}$ with Eq. (2.9) and $\vec{J}$ with Eq. (2.9) one gets respectively:

$$\vec{B} \cdot \nabla p = 0 \qquad (2.12)$$

$$\vec{J} \cdot \nabla p = 0 \qquad (2.13)$$

These mathematically computed relations physically imply that both the current and the magnetic field are perpendicular to the pressure gradient. This means that surfaces of constant pressure are also magnetic surfaces and therefore can be made of, but never crossed by, magnetic lines of force. Similarly, the current flows in and never across surfaces of constant pressure. In a tokamak geometry, these constant pressure surfaces are nested tori [3] as shown in Fig 2.1 below.
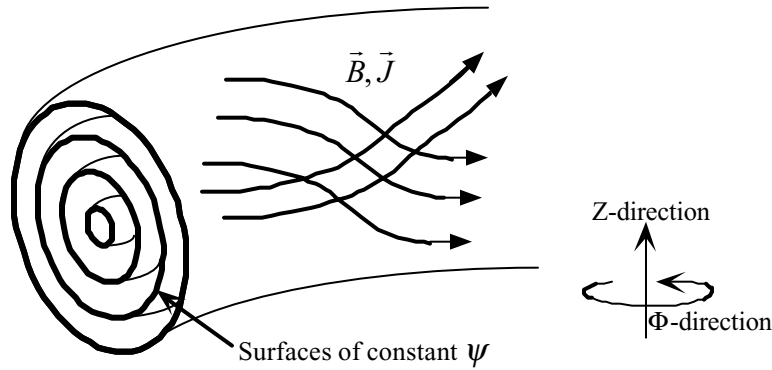
Fig 2.1 Nested tori of constant pressure surfaces (flux surfaces) on which B and J vectors lie

Ideal MHD equilibrium as it applies to tokamaks is a two-dimensional problem because of symmetry in the toroidal direction. In formulating this axisymmetric equilibrium a flux function $\psi(R, Z)$ is introduced satisfying Eq. (2.11) such that

$$B_R = -\frac{1}{R}\frac{\partial \psi}{\partial Z} \qquad (2.14)$$

19

$$B_Z = \frac{1}{R}\frac{\partial \psi}{\partial R} \tag{2.15}$$

$$B_\phi = B_\phi(R, Z) \tag{2.16}$$

where (R, ϕ, Z) are the usual cylindrical coordinates. Substituting Eqs. (2.14)-(2.16) into Ampere's law (Eq. (2.10)) gives the following expression for the current density

$$\mu_0 \vec{J} = -\frac{1}{R}\Delta^*\psi\hat{e}_\phi + \frac{1}{R}\nabla(RB_\phi)\times\hat{e}_\phi \tag{2.17}$$

where $\hat{e}_\phi$ is the unit vector in the toroidal direction and Δ^* is defined as

$$\Delta^* \equiv R\frac{\partial}{\partial R}\left(\frac{1}{R}\frac{\partial}{\partial R}\right) + \frac{\partial^2}{\partial Z^2} \tag{2.18}$$

Next, substituting Eqs. (2.14)-(2.18) into the force balance equation (Eq. (2.9)) yields the equilibrium equation for toroidally axisymmetric systems:

$$\Delta^*\psi = -\mu_0 R^2 \frac{dp(\psi)}{d\psi} - F(\psi)\frac{dF(\psi)}{d\psi} \tag{2.19}$$

where $F(\psi) \equiv RB_\phi$ and $p(\psi)$ are two surface quantities and free functions to be specified. Equation (2.19) is known as the Grad-Shafranov equation [4,5]. It is a second-order nonlinear partial differential equation describing axisymmetric toroidal equilibria. The nature of the equilibria is determined by the choice of the two free functions $p(\psi)$, $F(\psi)$ and boundary conditions. These functions are either measured (complicated in tokamaks) or modeled using empirical transport relations.

2.4 Linearized MHD stability

In order to study the stability of a plasma, the classical approach is to start with an MHD equilibrium, slightly perturb the configuration and examine whether the amplitudes of the

perturbations grow or decay with time. The starting point is the set of ideal MHD equations assuming no fluid equilibrium flow ($\vec{v} = 0$) and no electric field parallel to the boundary of the system ($E_{ll} = 0$). These non-linear equations are linearized by considering an arbitrarily small perturbation from the stationary equilibrium. Each relevant, non neglected quantity will consist of an equilibrium part (usually written with the subscript 0) and a perturbed part (usually written with the subscript 1). For example pressure p will have the form $p = p_0 + p_1$ where p_0 and p_1 are the equilibrium and perturbed pressure quantities respectively. The resulting linearized equation of motion (Eq. (2.2)) becomes:

$$\rho_0 \frac{\partial \vec{v}_1}{\partial t} = -\nabla p_1 + \vec{J}_0 \times \vec{B}_1 + \vec{J}_1 \times \vec{B}_0 \tag{2.20}$$

2.4.1 Plasma displacement

A useful transformation can be made by expressing the linearized equations in terms of the *displacement vector* $\vec{\xi}$ that represents the flow of fluid elements past a stationary point [2]. It is defined as

$$\vec{\xi}(\vec{x}, t) \equiv \int_0^t v_1(\vec{x}, t') dt' \tag{2.21}$$

where v_1 is the perturbed velocity and the perturbation is vanishingly small. Other perturbed variables can also be related to $\vec{\xi}$. This gives the following:

$$\vec{B}_1(\vec{x}, t) = \nabla \times \left(\vec{\xi} \times \vec{B}_0 \right) \tag{2.22}$$

$$p_1(\vec{x}, t) = -\vec{\xi} \times \nabla p_0 - \gamma p_0 \nabla \cdot \vec{\xi} \tag{2.23}$$

The linearized equations may then be combined by substituting Eqs. (2.22), (2.23) and (2.10) into Eq. (2.20) and the resulting equation of motion becomes

21

$$\rho_0 \frac{\partial^2 \vec{\xi}}{\partial t^2} = \vec{F}\left(\vec{\xi}\right) \qquad (2.24)$$

where $\vec{F}\left(\vec{\xi}\right)$ is the force function due to a plasma displacement $\vec{\xi}$. $\vec{F}\left(\vec{\xi}\right)$ has the form

$$\vec{F}\left(\vec{\xi}\right) = \nabla\left(\gamma p_0 \nabla \cdot \vec{\xi} + \vec{\xi} \cdot \nabla p_0\right) \qquad (2.25)$$

$$+ \frac{1}{\mu_0}\left(\nabla \times \left[\nabla \times \left(\vec{\xi} \times \vec{B}_0\right)\right]\right) \times \vec{B}_0$$

$$+ \frac{1}{\mu_0}\left(\nabla \times \vec{B}_0\right) \times \left[\nabla \times \left(\vec{\xi} \times \vec{B}_0\right)\right]$$

In principle, given an initial perturbation $\vec{\xi}$ applied to an equilibrium and some boundary conditions, Eqs. (2.24) and (2.25) can be used to determine the dominant unstable mode. This method is called the initial value method.

If the perturbation $\vec{\xi}$ has the form $\vec{\xi}(\vec{x}, t) = \vec{\xi}(\vec{x})\exp(-i\omega t)$, the equation of motion Eq. (2.24) becomes an eigenvalue formulation stated as follows

$$-\omega^2 \rho \vec{\xi} = \vec{F}\left(\vec{\xi}\right) \qquad (2.26)$$

The advantage here is that only the boundary conditions need to be specified. An eigenvalue $\omega^2 > 0$ gives stable oscillatory solutions. An eigenvalue $\omega^2 < 0$ means the frequency has the form $\omega = i\gamma$. If $\gamma > 0$, the eigenmode is unstable, and when $\gamma < 0$, it is stable.

2.4.2 The energy principle

The physical basis for the energy principle [6] is the fact that energy is conserved in the ideal MHD model. Any changes in the potential energy of an equilibrium plasma must be compensated by corresponding changes in the kinetic energy in a manner that conserves total

energy. The functional used to account for potential energy changes due to a plasma

displacement $\vec{\xi}(\vec{x})$ is the volume integral

$$\delta W = \frac{1}{2} \int \vec{\xi}(\vec{x}) \cdot \vec{F}\left(\vec{\xi}\right) d^3 x \qquad (2.27)$$

where a negative δW, for any permitted $\vec{\xi}(\vec{x})$, means instability. The kinetic energy functional is

the volume integral

$$K\left(\vec{\xi}^*, \vec{\xi}\right) = \frac{1}{2} \int \rho_0 \vec{\xi}^* \cdot \vec{\xi} d^3 x \qquad (2.28)$$

The problem is usually expressed in variational form and the unstable modes are the

eigenfunctions that correspond to an extremum of the Lagrangian

$$L = \omega^2 K\left(\vec{\xi}^*, \vec{\xi}\right) - \delta W\left(\vec{\xi}^*, \vec{\xi}\right) \qquad (2.29)$$

This is the method used in the PEST-I [7] linear ideal MHD stability code.

2.5 The external kink mode

The most dangerous instability on HBT-EP and other tokamaks is the external kink

mode. This mode has fast growth rates, a global structure and usually alters the plasma

boundary. These properties change when the separation between HBT-EP's close fitting wall

and the plasma surface is modified. This section outlines important issues and results of linear

ideal MHD theory as they relate to the external kink.

2.5.1 Large aspect ratio expansion

The aspect ratio of a toroidal device is the ratio of its major radius to its minor radius. It

is defined as

$$\varepsilon^{-1} \equiv \frac{R}{a} \tag{2.30}$$

where ε is known as the inverse aspect ratio and is a dimensionless quantity.

It has been shown [8,9] that δW can be expanded in orders of ε for a low-β tokamak assuming a large aspect ratio. The first destabilizing contribution comes in the second order term of the expansion, to which the external kink mode is associated. Starting with a perturbation that is $\propto \exp i(m\theta - n\phi)$, with m and n respectively the poloidal and toroidal mode integer numbers; noting the plasma radius a and b the radius of a conducting wall surrounding the plasma, with a vacuum between them, the resultant potential energy functional has the form

$$\frac{R_0}{\pi^2 B_\phi^2} \delta W = \int_0^a \left[\left(r \frac{d\xi}{dr} \right)^2 + (m^2 - 1)\xi^2 \right] \left(\frac{n}{m} - \frac{1}{q} \right)^2 r\,dr \tag{2.31}$$

$$+ a^2 \xi_a^2 \left[\frac{2}{q_a} \left(\frac{n}{m} - \frac{1}{q_a} \right) + (1 + m\lambda) \left(\frac{n}{m} - \frac{1}{q_a} \right)^2 \right]$$

Here the subscript a implies the quantities are evaluated at the plasma boundary, and λ is

$$\lambda = \left[1 + (a/b)^{2m} \right] \Big/ \left[1 - (a/b)^{2m} \right] \tag{2.32}$$

2.5.1.1 Effect of a conducting wall

If there is no vacuum region between the plasma and its surrounding wall $(b = a)$, the fluid cannot displace and $\xi_a = 0$. Substituting in Eq. (2.31) yields a $\delta W > 0$ for all modes with $m > 1$, hence stability for all perturbations with a poloidal mode number greater than one. When $m = 1$ with $b = a$, there is an internal kink instability that has a reduced growth rate relative to the external mode [8].

In practice, having a super conducting wall that completely surrounds the plasma surface is not compatible with thermonuclear fusion. The next best option is a *non ideal* wall, that will have some resistivity and will only partially cover the plasma surface.

a) Finite wall resistivity

There are several theories and models that examine the consequence of finite wall resistivity on MHD modes [1,10,11].

Ideal MHD theory with a resistive wall shows that the growth time of the external kink mode can only be slowed down from the ideal time scale, τ_{ideal} ($\approx 10\mu s$ for HBT - EP) to the time scale of the resistive wall, $\tau_{L/R}$ ($\approx 10ms$ for HBT - EP).

Recent numerical and analytical studies [12,13,14,15] show that with external kink-unstable rotating plasmas surrounded by a conducting wall, the slowly growing *resistive wall mode* can be stabilized. This mode *penetrates* the resistive wall and is nearly locked to it, rotating with respect to that wall at a *slip* frequency much smaller than the plasma rotation frequency. If the slip frequency is sufficiently rapid the resistive wall mode is stable. The theory of resistive wall modes of ideal plasmas has predicted the possibility of achieving complete stability of external kink modes. For that, the plasma rotation velocity should be sustained beyond the critical velocity.

b) Partial wall effects

Another discrepancy between perfect models and experiments arises when considering the extent of wall coverage around the plasma surface. Theoretical studies assume a toroidally continuous conducting wall. In practice, this cannot be achieved. For example, HBT-EP's conducting wall has both toroidal and poloidal gaps. These discontinuities modify the image

currents flowing in the conducting wall sections and distort the eddy current patterns which stabilize MHD modes.

A detailed investigation of the effects of conducting wall symmetry on wall stabilization is being carried out on HBT-EP [16].

2.5.1.2 The *m=1* limit

If the wall is away from the surface of the plasma, a constant $\xi(r)$ is the eigenfunction that minimizes the energy functional δW for the $m = 1$ mode. Therefore for a bulk displacement of the plasma column $(\xi(r) = const)$ and a worst case scenario of $n = 1$ and $m = 1$, the condition for stability is

$$q_a > 1 \tag{2.33}$$

This is the Kruskal-Shafranov [17,18] stability criterion which imposes a limit on the maximum allowable current in a tokamak with a given toroidal field. In practical situations, the *m=1* external kink is difficult to observe experimentally because higher m modes pose even stronger requirements on q_a.

2.5.1.3 m=2 (external kinks)

In general, the *m=2* external kinks impose more restrictive conditions on q_a and the current profile than those corresponding to the m=1 mode. A stability criterion for general m, n, is $q_a > m/n$. This assumes that q monotonically increases with r, which is valid in most tokamaks including HBT-EP. The implication here is that modes having resonant surfaces within

26

the plasma will be stable. Also a low limit is imposed on the toroidal current for high-m, low-n modes, which is not very useful.

Shafranov [8] obtained a slightly improved stability estimate for a flat current profile, no conducting wall and choosing $\xi(r) = const \times r^{m-1}$ as a minimizing perturbation for the energy functional δW. The resulting regions of stability for a given m and n are bound by $(m-1)/n \leq q_a \leq m/n$. For the n=1 case, this implies instability over the entire range of q_a. This pessimistic result strongly depends on the chosen shape of the current profile. The flat current model, with its infinitely steep edge gradient, is unrealistic since the plasma current usually goes smoothly to zero at the plasma surface. For the more practical profiles, the stability properties are more optimistic. In essence, as m increases, the mode structure for external kinks becomes more localized in the vicinity of the plasma edge. The destabilizing contribution to δW becomes sensitive to the local behavior of $J(r)$, the current density, near the plasma surface and when $J(a)$ and $J'(a)$ are small, the instabilities diminish. This is in contrast to the m=1 instability that depends only on the total current.

The above results were examined [19,1,20] analytically and the unstable regions were calculated for the following two cases

$\underline{J(a) = J_a \neq 0}$

Instabilities are predicted to appear bounded by

$$\frac{1}{n}\left(m - \frac{J_a}{\langle J \rangle}\right) \leq q_a \leq \frac{m}{n} \tag{2.34}$$

where J_a is the current density at r=a and $\langle J \rangle$ is the average current density in the plasma.

Here, any profile with a current jump at the surface of the plasma is unstable to high m external

kinks over bands of q_a values as illustrated in Fig 2.2 [1]. For a uniform current profile, with
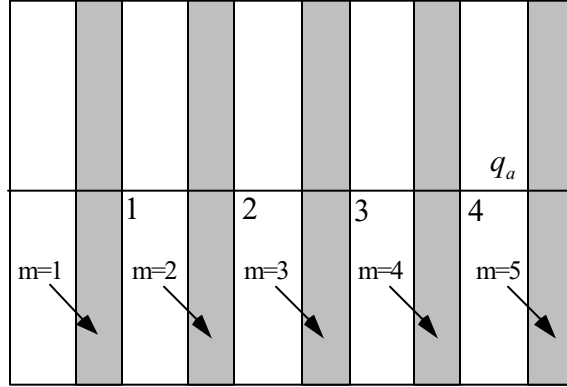
Fig 2.2 Stability diagram showing bands of instability.
The shaded areas represent regions of unstable q_a

$J_a/\langle J \rangle = 1$, the previous most unstable result is retrieved.

$\underline{J_a = 0}$

For this case, the instability boundaries have the more complicated form

$$\frac{1}{n}\left[m - \exp\left(\frac{2m\langle J \rangle}{aJ_a'} \right) \right] < q_a < \frac{m}{n} \tag{2.35}$$

Here, the instability only exists over exponentially narrow bands of q_a. The conclusion is that

when the current vanishes at r=a the range of unstable q_a values is reduced.

Wesson [9] shows the general effect of the current gradient on kink stability by

choosing a family of profiles $J = J_0\left(1 - r^2/a^2\right)^{\nu}$ with ν as the steepness factor. The safety

factor is given by $\nu + 1 = q_a/q_0$ where the subscript 0 refers to the value on axis. The results of

Wesson's calculations are illustrated in Fig 2.3 taken from his paper [9]. With respect to

external kinks, for $\nu > 2.5$ all m=2 modes are stable for all $q_a > 1$. Internal mode stability

considerations require $q_0 > 1$. If the ideal constraint of perfect conductivity is relaxed, the stable

space is further reduced by the inclusion of *tearing* modes. These are resistive modes driven by

the current density gradient with resonant surfaces inside the plasma and lower growth rates

than ideal mode.

Fig 2.3 Wesson stability diagram for a large aspect ratio, low beta plasma of circular cross-section

2.5.2 Effects of finite beta

Using the surface current model (all currents flow on the surface of a constant-pressure

plasma, surrounded by a vacuum region, and pressure is constant within the plasma), Friedberg

and Haas [21] analytically examine the stability of high-β equilibria to external modes. They find

that among all the contributions (plasma, surface of the plasma and vacuum) to the energy

functional δW, the destabilizing term is the surface one. It is expressed as

$$\delta W_s = -\frac{\pi \varepsilon^2 B_0^2 R_0}{\mu_0} \int_0^{2\pi} d\theta |\xi|^2 \left[\left(\frac{B_\theta(a,\theta)}{\varepsilon B_0} \right)^2 + \left(\frac{\beta}{\varepsilon} \right) \cos\theta \right] \tag{2.36}$$

The first term in the integral corresponds to the usual current drive kink mode. The second term

corresponds to the effects associated with toroidicity and plasma pressure. It is strongest on the

29

outside of the tokamak $\left(\theta = 0°\right)$ and the resulting unstable mode shows a larger displacement in this region. This indicates that pressure driven modes are ballooning in nature (i.e. localized on the outboard side of the torus).

2.5.3 Troyon limit

In order to do a detailed analysis of MHD stability for tokamak equilibria, it is necessary to solve the MHD equations numerically. Troyon *et al*. [22] examined the boundaries of ideal MHD instabilities as they relate to β values in tokamaks. The analysis was done numerically and consisted of optimizing pressure and current profiles for a variety of equilibria. The most restrictive mode on the achievable β-limit is the n=1 external kink. The stability boundary is described by a simple formula referred to as the Troyon limit. It is based on measurable quantities and is expressed as $\beta_N \le C_T$. Here C_T is a constant that depends on geometry and profile parameters. It is on the order of three with no wall stabilization (conducting wall at infinity). A similar scaling for the MHD stability limit of high-n ballooning modes [23] has been shown with a constant on the order of four. In general, the β-limit presented by kink modes is lower than the one set by ballooning modes and is therefore responsible for the operational β-limit in tokamaks.

References

[1] J. Friedberg, *Ideal Magnetohydrodynamics* (Plenum press, NY 1987).

30

[2] G. Bateman, *MHD Instabilities* (MIT press, Cambridge, 1978).

[3] M.D. Kruskal and R.M. Kulsrud, Physics of Fluids **1** 253 (1958).

[4] H. Grad and H. Rubin, Proceedings of the 2nd United Nations Conference on the Peaceful Uses of Atomic Energy (Geneva) **31** 190 (Columbia University press, NY 1959).

[5] V.D. Shafranov, Zhurnal Experimentalnoi i Teoretticheskoi Fiziki **33** 710 (1957). [Soviet Physics J.E.T.P. **6** 545 (1958)].

[6] I.B. Bernstein et al., Proc. R. Soc. London, Ser. A **244** 17 (1958).

[7] R.C. Grimm, J.M. Greene and J.L. *Johnson, Methods in Computational Physics* **16** 253 (Academic press, NY 1976).

[8] V.D. Shafranov, Zhurnal Experimentalnoi i Teoretticheskoi Fiziki **40** 241 (1970). [Soviet Physics J.E.T.P. **15** 175 (1970)].

[9] J.A. Wesson, Nuc. Fusion **18** 87 (1978).

[10] R. Fitzpatrick, Physics of Plasmas **1** 2931 (1994).

[11] J. Friedberg, *Workshop on the Stabilization of the External Kink and other MHD issues* (San Diego, CA, June 23-25, 1993).

[12] A. Bondeson and J.D Ward, Phys. Rev. Lett. **72** 2709 (1993).

[13] N. Pomphrey et al., Plasma Physics and Controlled Nuclear Fusion Research **1994** IAEA, Seville (1994).

[14] R. Betti and J. Friedberg, Phys. Rev. Lett. **74** 2949 (1995).

[15] R. Fitzpatrick and A. Aydemir, U. Texas at Austin Report **694** (1995).

[16] E. Eisner, Ph.D. thesis, Columbia University, 1997.

[17] M.D. Kruskal et al., Physics of Fluids **1** 421 (1958).

[18] V.D. Shafranov, Plasma Physics and the Problem of Controlled Thermonuclear Reactions **1** (Pergamon press, NY 1958).

[19] G.Laval et al., Physics of Fluids **17** 835 (1974).

[20] G. Eriksson and C. Wahlberg, Phys. Rev. Lett. **72** 2713 (1994).

[21] J. Friedberg and F.A. Haas, Physics of Fluids **16** 1909 (1973).

[22] F. Troyon et al., Plasma Physics and Controlled Fusion **26** 209 (1984).G

[23] A. Sykes et al., Controlled Fusion and Plasma Physics (EPS, Aachen, 1983).

Chapter 3
DISRUPTION REVIEW

This chapter describes disruption phenomena and gives a synopsis of the present understanding of the subject. The sections outline important topics related to disruptions and present a guide to significant references. Both theoretical and experimental results are covered.

3.1 Sawtooth oscillations

Sawtooth oscillations were discovered in the ST tokamak by Von Goeler *et al* [1]. It was noticed that in a stable phase of a plasma discharge, the central temperature experienced periodic oscillations of relaxation type. Since then, sawtooth oscillations have been observed in practically all tokamaks, including HBT-EP.

The sawtooth process consists of periodically repeated phases. First, the temperature at the center of the plasma column slowly rises, then quickly drops. Shortly before each temperature drop (sometimes called *a crash*), *precursor* oscillations of the $m=1$ type are observed. The thermal collapses associated with sawteeth flatten the temperature profile inside some radius $r < r_{inv}$ and increases the temperature outside this radius ($r > r_{inv}$). The r_{inv} radius is called the inversion radius and the corresponding temperature profile flattening is sometimes called an *internal disruption*.

One of the earliest theoretical explanations of sawtooth oscillations comes from Kadomtsev [2]. He speculates that the central safety factor, $q(0)$, drops below unity prior to the sawtooth. At the inversion radius, $q(r_{inv})=1$. Within $r < r_{inv}$, an internal $m=1$, $n=1$ mode

develops and locally compresses the magnetic field at the helical resonant surface, q=1, leading to a reconnection of the magnetic field lines. More recent models have refined the Kadomtsev picture by including the growth of an *m=1* tearing mode [3-5] and stochastic field lines [6].

Sawtooth oscillations are an important non-linear MHD instability. They are noticeable because they result in rapid mixing of the plasma thermal energy. They are also the starting point of the understanding of a more dangerous tokamak phenomenon: the disruptive instability .

3.2 The disruptive instability

The disruptive instability was observed in the earliest phase of experiments in tokamaks [7,8]. The first observations indicated major common characteristics of the event: negative spike on the measured voltage drop across the toroidal plasma current, positive current derivative and drastic decrease of the plasma major radius. These observations were consistent with a broadening of the current-carrying region followed by a partial release of the poloidal flux from the plasma. Disruptions are usually preceded or accompanied by strong MHD oscillations and plasma energy loss. The disruptive instability may lead to total loss of plasma current; such a disruption is called a *major disruption*. There are also *minor disruptions*: partial loss of energy from the plasma without total destruction of the ability to maintain the plasma current. Examples of disruptions on HBT-EP are analyzed in chapter six. Both minor and major disruptions together with the internal disruption as manifested by sawtooth oscillations represent similar behavior. However, they evolve on different time scales. A comparison of the characteristics of these three types of disruptions is shown in table III.1 [9].
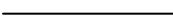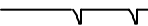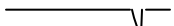
34
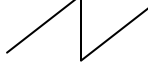
Types of disruption	Saw-tooth	Minor disruption	Major disruption
V(t) Voltage ΔV	time "t" ——	time "t" -1 to -10 V	time "t" -10 to -200 V
$\chi(t)$ Soft x-ray $\Delta\chi$	$\approx 10\%$	$\approx 20 - 80\%$	Drop by several times
$\Delta T_e(0)$	$\approx 10\%$	$\approx 20 - 50\%$	$\approx 90\%$
Δn_e	$\approx 1 - 4\%$	$\approx 10\%$	$\approx 30\%$
$\tilde{B}_\theta / B_\theta$	——	$\leq 4\%$	$\approx 15 - 20\%$
m	1, 0 time "t"	(3), 2, 1, (0) time "t"	(3), 2, 1, 0, 3, 4 time "t"

Table III. 1 Comparative characteristics of different disruptions

Major disruptions are dangerous since, as mentioned earlier in chapter one, they can potentially damage large tokamaks or future generation devices if they are not controlled. The large electromagnetic forces associated with current and energy quenches can result in large mechanical forces and stresses that may destroy mechanical structures of machines. Also, rapid energy losses may bring damaging heat and particle fluxes to nearby limiters, divertors and walls.

Disruptions can develop in tokamaks near the operational density, current or β limits or they can be initiated by other conditions associated with the mishandling of plasmas such as (1)

fast current or density rises; (2) changing geometry from a limiter to a divertor; (3) very large "sawtooth" oscillations especially at high current; (4) mode activity localized at the plasma edge; and (5) penetration of fragments from the first wall into the plasma. The circumstances of plasma destabilization are varied but the scenarios of disruptions are more or less similar and widely known experimentally [10-14].

Tokamaks have a preferred operating space in which the plasmas are stable. In a quiet discharge phase, disruptions start to develop while approaching the operating limits. Correspondingly, three experimentally different limits are often singled out as the most important.

3.3 Density limit disruptions

It is generally agreed that density limit disruptions [14-17] are caused by radiative cooling of the edge bringing about the shrinking of the current channel [18]. As the central current gradients become steep, a strong internal kink develops which injects a "cold bubble" into the center of the plasma [19, 20].

3.4 Low-q* disruption limit

The high current or low-q* disruptive instability has been observed and examined on several tokamaks [12,14,21-24]. The disruptions occur as a result of raising the current to a level where MHD instabilities, such as external kinks, rapidly grow causing energy losses and current decays. The current is limited to $q^* \geq 2$ in a circular cross section plasma. However,

tokamaks with elongated cross-sections (JET, DIII-D and PBX-M) have operated with $q*$ below 2 but always above 1 [25].

3.5 β − limiting disruptions

The disruptive limit to high-β operation in a tokamak has been identified and studied extensively [21,26-29]. At high-β, increased pressure gradients lead to the appearance of MHD instabilities as a prelude to the destruction of the discharge. Three types of MHD instabilities may arise: high-n internal modes, also known as ballooning modes [30-32], low-n internal modes, sometimes called "infernal" modes [33] and finally low-n external modes, specially external kink modes [34,35] which pose the most severe limit to achieving high-β. Most β-limit results have been obtained with neutral beam injection heating and either low magnetic field or low current [25].

On TFTR, MHD precursor modes associated with disruptions at high-β have been identified as external kinks with a fast growth time of less than $50\,\mu s$. They are visible only prior to the thermal quench phase [36].

An operational beta limit of $\beta_N = \beta/(I/aB) \le 3.5$ has been encountered in DIII-D. Figure 3.1 shows that the maximum achievable beta scales linearly with I/aB over a factor of 3. When the degradation of energy confinement occurs at high β_N, it is correlated with the presence of low-n MHD instabilities [27]. The disruptions are sudden, a non rotating ideal kink mode with m/n=2/1 appears within $50\,\mu s$ after a sawtooth collapse. A rapid loss of plasma energy occurs in the presence of this mode, beginning at the edge and becoming complete within one to two milliseconds

Fig 3.1 Beta versus I/aB for DIII-D beam heated discharges (ref 27)

The disruptive β-limit in PBX [37] is above the n=1 kink mode limit in the absence of a conducting wall. It is consistent however with the predicted beta limit for n=1 kink modes with a conducting wall at roughly the position of the vacuum vessel as seen in Fig 3.2. Because of such observations, the addition of a set of close-fitting conducting plates near the plasma surface to help stabilize the n=1 kink mode has been implemented in several tokamak experiments and is part of reactor designs [38].
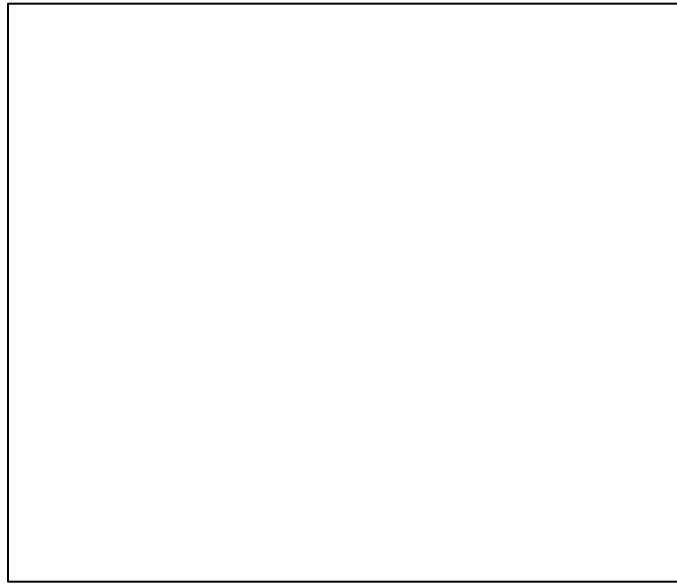
**Fig 3.2 Operating range of high beta discharges in PBX compared
to calculated ideal stability limits with and witout a conducting wall (ref 37)**

3.6 Tokamaks with conducting walls

The stabilization of long wavelength external modes that appear at high-β such as external kinks was investigated and the use of a conducting wall near the surface of the plasma was found to be the most effective. In that area, ideal wall stabilization [34] and non-ideal effects, namely finite resistivity of conducting walls [34, 39-41] and partial wall coverage [41] have been studied and are still an active area of research. Non-MHD effects on the stability of a mode with the presence of a wall are also being examined [40, 42]. There are also theories about an optimal plasma-wall separation that will best suppress the instabilities and permit achievement of high-β values [41].

Besides HBT-EP at Columbia, the PBX-M tokamak at Princeton and the DIII-D tokamak at General Atomics are the only two experiments in the US that have studied wall stabilization.

3.6.1 PBX-M

The installation of a fixed conducting wall improved performance in the modified Princeton Beta Experiment (PBX-M) [37] over that obtained in the predecessor device PBX [43]. Results from PBX-M have shown evidence of wall stabilization of modes and increased stabilization due to mode rotation. Also PBX-M reports higher current levels or lower edge-q discharges because of the presence of their conducting wall [44].

Recent work showed that high-β disruptions precursors have a strong dependence on the coupling between the plasma and the conducting plate [45]. Measured growth rates varied between $100 \, \mu s$ up to $20 \, ms$ as a function of wall position. The behavior of the observed disruption precursors were interpreted in terms of the resistive wall mode theory of ideal plasmas.

3.6.2 DIII-D

The observed β-limit in DIII-D is higher than the β-limit predicted in the absence of a perfectly conducting wall. Detailed analysis of high beta discharges demonstrates that the resistive vacuum vessel can provide stabilization of low-n MHD modes. The experimental beta values reaching up to $\beta_T = 12.6\%$ are more than 30% larger than the maximum stable beta calculated with no wall stabilization. Currently, more experiments are planned to address mode rotation and resistive wall modes issues [46,47].

3.6.3 HBT-EP

The HBT-EP device is also able to examine wall stabilization. Understanding the influence of the close fitting conducting walls on different disruptions as they occur and documenting the effects of changing the plasma-wall separation should provide new results and needed guidance to the next generation tokamaks.

References

[1] S. Von Goeler et al., Phys. Rev. Lett. **33** 1201 (1974).

[2] B. Kadomtsev, Soviet Journal of Plasma Physics **1** 389 (1975).

[3] G. Jahns et al., Nuc. Fusion **18** 609 (1978).

[4] B. Kadomtsev, Plasma Physics and Controlled Fusion **26** 217 (1984).

[5] W. Pfeiffer, Nuc. Fusion **25** 673 (1985).

[6] M. Dubois and A. Samain, Nuc. Fusion **20** 1101 (1980).

[7] E.P. Gorbunov and K.A. Razumova, Atomic Energy (in russian) **15** 363 (1963).

[8] L.A. Artsimovich, Nuc. Fusion **12** 215 (1972).

[9] B. Kadomtsev, *Tokamak Plasma: A Complex Physical System* (Plasma Physics Series, Institute of Physics Publishing, Bristol & Philadelphia, 1992).

[10] Equipe TFR, Nuc. Fusion **17** 1283 (1977).

[11] N. Sauthoff et al., Nuc. Fusion **18** 1445 (1978).

[12] S. Tsuji et al., S. Kawahata et al., Nuc. Fusion **25** 305 (1985).

[13] D. Campbell et al., Plasma Physics and Controlled Nuclear Fusion Research **1986** IAEA, Vienna (1986).

[14] J.A. Wesson et al., Nuc. Fusion **29** 641 (1989).

[15] M. Murakami et al., Nuc. Fusion **16** 347 (1976).

[16] M. Greenwald et al., Nuc. Fusion **28** 2199 (1988).

[17] V. Alikaev et al., Plasma Physics and Controlled Nuclear Fusion Research **1990** IAEA, Washington DC (1990).

[18] D. Ward and J.A. Wesson, Nuc. Fusion **32** 1117 (1992).

[19] R. Kleva and J. Drake, Physics of Fluids B **3** 372 (1991).

[20] A. Bondeson et al., Nuc. Fusion **31** 1695 (1991).

[21] G. Jahns et al., Nuc. Fusion **28** 881 (1988).

[22] J. Snipes et al., Nuc. Fusion **28** 1085 (1988).

[23] M. Nagami et al., Nuc. Fusion **22** 409 (1982).

[24] TFR group, Nuc. Fusion **24** 784 (1984).

[25] B.B. Kadomtsev et al., Nuc. Fusion **30** 1675 (1990).

[26] F. Troyon et al., Plasma Physics and Controlled Fusion **26** 209 (1984).

[27] E. Strait et al., Plasma Physics and Controlled Nuclear Fusion Research **1988** IAEA, Nice (1988).

[28] M. Mauel et al., Plasma Physics and Controlled Nuclear Fusion Research **1988** IAEA, Nice (1988).

[29] Jet Team, Plasma Physics and Controlled Nuclear Fusion Research **1990** IAEA, Washington DC (1990).

[30] C. Mercier et al., Plasma Physics and Controlled Nuclear Fusion Research **1978** IAEA, Nice (1978).

[31] B. Coppi et al., Nuc. Fusion **19** 715 (1979).

[32] H.R. Strauss et al., Nuc. Fusion **20** 638 (1980).

[33] J. Manickam et al, Nuc. Fusion **27** 1461 (1987).

[34] J. Friedberg, *Ideal Magnetohydrodynamics* (Plenum press, NY 1987).

[35] E. Strait, Physics of Plasmas **1** 1415 (1994).

[36] E. Fredrickson et al., PPPL Report **3023** (1994).

[37] M. Okabayashi et al., Plasma Physics and Controlled Nuclear Fusion Research **1986** IAEA, Kyoto (1986).

[38] F. Najmabadi and R.W. Conn, Plasma Physics and Controlled Nuclear Fusion Research **1992** IAEA, Würtzburg (1992).

[39] J.P. Goedbloed et al., Nuc. Fusion **12** 649 (1972).

[40] J. Snipes et al., Nuc. Fusion **28** 1085 (1988).

[41] R. Fitzpatrick, Physics of Plasmas **1** 2931 (1994).

[42] A. Bondeson and J.D Ward, Phys. Rev. Lett. **72** 2709 (1993).

[43] R. Bell et al., Physics of Fluids B **2** 1271 (1990).

[44] M. Okabayashi et al., Plasma Physics and Controlled Nuclear Fusion Research **1988** IAEA, Nice (1988).

[45] M. Okabayashi et al., PPPL Report **3168** (1996).

[46] A. Turnbull et al., Plasma Physics and Controlled Nuclear Fusion Research **1994** IAEA, Seville (1994).

[47]] T. Taylor et al., Physics of Plasmas **2** 2390 (1995).

Chapter 4
THE HBT-EP EXPERIMENT

This chapter describes the hardware components of the HBT-EP experiment. It is a summary, more details can be found in [1].

4.1 Coil systems

HBT-EP utilizes the toroidal field coils from the CLEO tokamak/stellerator in Culham laboratories [2]. A fast ohmic heating system enables rapid discharge startup. A flexible poloidal field coil system permits control of plasma position and shape.

4.1.1 Toroidal field (TF) system

The toroidal field (TF) coils are a set of twenty 64 turn copper coils (each coil consists of two 32 turn coils, side by side) which rest inside stainless steel dewers which in turn are surrounded by large aluminum casings. The total inductance of these coils is 0.235H with a resistance of 0.635? . A 10kV, 0.04 Farad (2MJ) capacitor bank powers these magnets. The peak field that is attainable with the current TF system is 0.5 Tesla. Figure 4.1 is a top view showing the TF coils, transformer coils, vacuum vessel and the locations of various diagnostics. The twenty TF coils are grouped into ten coil pairs each linked by one of the ten large vacuum chamber segments (described later in the chapter). This modular arrangement allows each chamber/magnet pair to be handled separately, facilitating maintenance and disassembly. The centering forces on the TF coils due to higher field on the inside of the torus are opposed by a central cylinder made of aluminum and G-10 fiber glass epoxy composite material. The

moments arising from the interaction of the vertical field and the TF currents are taken up by large stainless steel turnbuckles between the coils. A dielectric fluid is circulated in the cavity originally used for liquid nitrogen for cooling purposes. The coil heat increase of $5°C$ at full energy (2MJ) is removed by chilling the fluid with a 23,000 Btu/hour chiller.

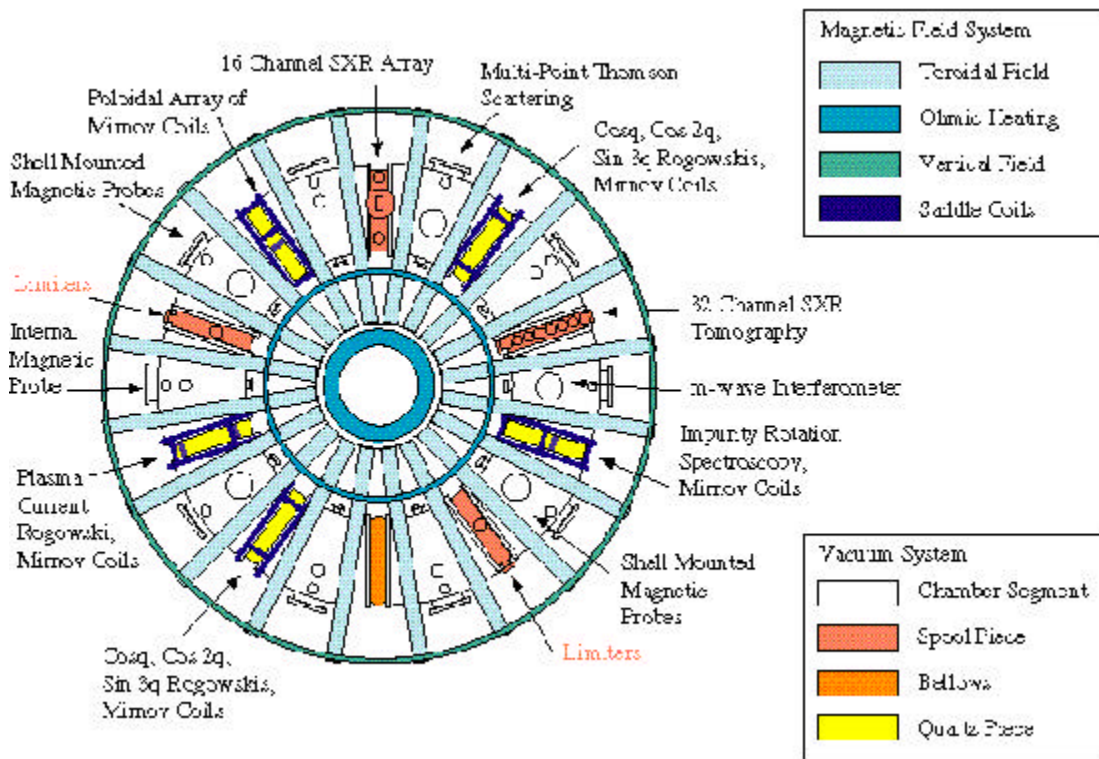**Fig 4.1 Top view of HBT-EP showing magnet configuration, vacuum chamber components and diagnostic location**

4.1.2 Poloidal field (PF) system

The poloidal field setup on HBT-EP [3] includes both the ohmic heating (OH) and the vertical field (VF) systems, see Fig 4.2. The OH transformer consists of a six turn air core coil set. The central four turns (OH1) are one unit, cast in an epoxy ceramic composite. The upper

45

and lower turns (OH2) are free standing copper coils mounted on the TF magnets. All the turns are fabricated from OFHC grade copper bars with a cross section of 0.5" by 3.5". The coil inductance is $15\mu H$.

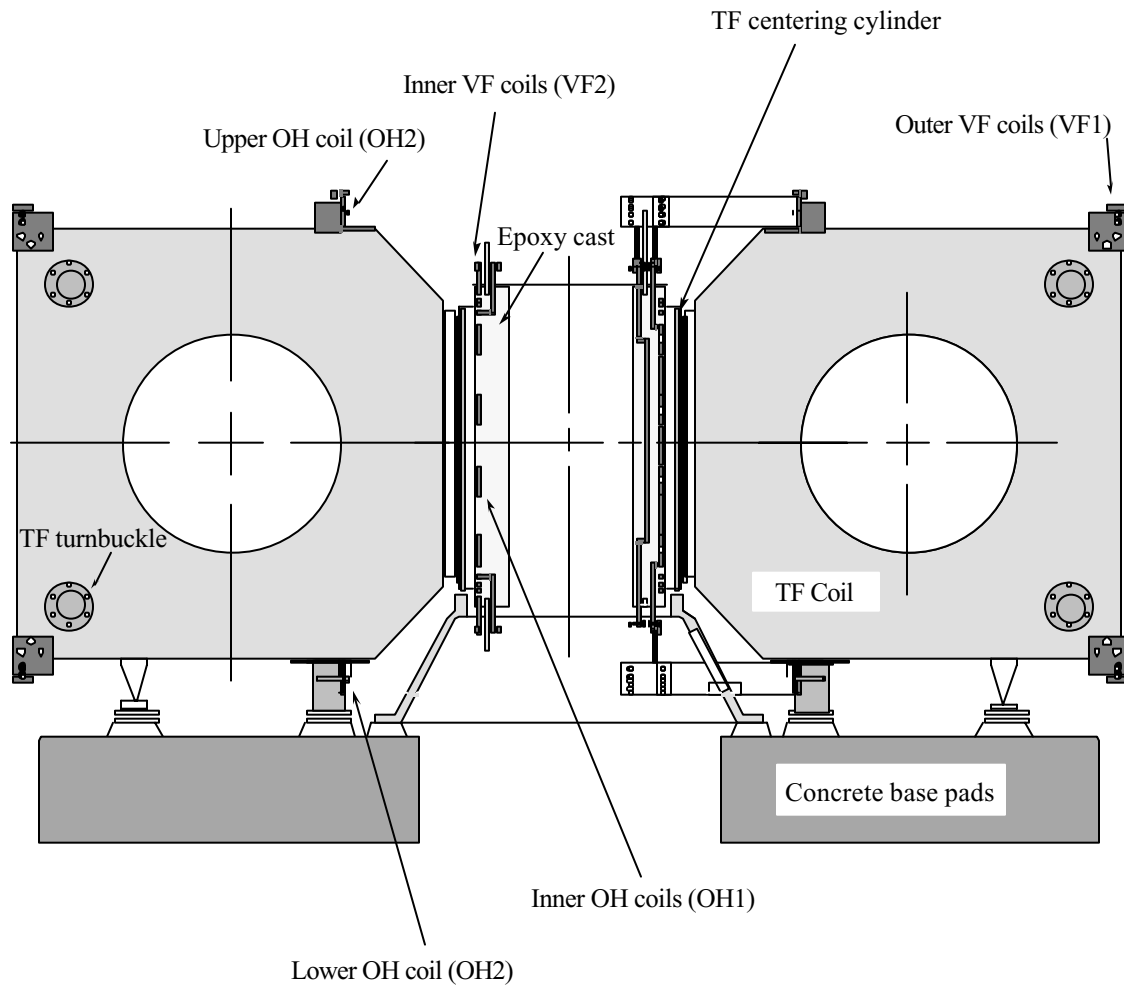**Fig 4.2 Cross sectional view of the HBT-EP principal coils**

The VF coils consist of two outer (VF1) two turn coils supported on the TF magnets and two inner (VF2) three turn compensation coils located in the epoxy cast of the OH coil. The outer coils are made of double strands welding cable and have a radius of 157 cm, with a vertical separation of 129 cm between them. The inner coils are made of OFHC grade copper

bars with a cross section of 0.5" by 0.5", they have a radius of 27 cm, with a vertical separation of 80 cm between them.

The VF2 sections potted with the OH1 coil are wound anti-parallel to the VF1 parts. The current in the inner coils flows in the opposite direction to the current in the outer coils. The purpose of these inner VF2 segments is to eliminate the mutual inductance between the VF and OH coils by making flux that opposes the coupled flux from the outer VF coils. The air core ohmic heating coil is built to minimize the poloidal field within the plasma and allows fast current start up with rise times of $\approx 100\,\mu s$.

The OH and VF coils are powered, similarly to the TF coils, by capacitor banks. Some details on their designs and construction can be found in reference [1]. In order to initiate a typical plasma discharge, the air core OH transformer is charged with a negative bias current (bias bank) with a rise time of $\approx 500\mu s$ followed by a fast start current (start bank) with a rise time of $\approx 150\,\mu s$, permitting the formation of the plasma discharge faster than the magnetic diffusion time. A one Farad electrolytic power crowbar sustains the loop voltage. A low power electron gun provides free electrons to aid in plasma breakdown. The VF bank (fast start bank followed by a power crowbar) is fired at the same time as the OH start bank.

4.2 Vacuum system

The HBT-EP vacuum chamber maintains an ultra high vacuum consistent with low impurity fraction specially oxygen control so as to achieve high temperature operation at the Troyon β-limit. The vacuum vessel also supports an adjustable conducting wall used for equilibrium and external kink stability. The chamber incorporates rapid soak-through of the

47

poloidal fields, reduction of the peak electric field during the breakdown of the plasma, good diagnostics access and easy assembly.

4.2.1 Vacuum vessel segments

The complete vacuum vessel is shown above in the top view schematic of HBT-EP, Fig 4.1. The vacuum chamber consists of ten large wedge shaped stainless steel segments, see Fig 4.3. These are made from standard 20" diameter 90° pipe elbows. Each of these ten segments are terminated by large stainless steel end flanges on either side. These are at an angle of 36° relative to each other. All the ports on the vessel use copper sealing gaskets so as to eliminate permeation of air that often occurs with O-ring seals.

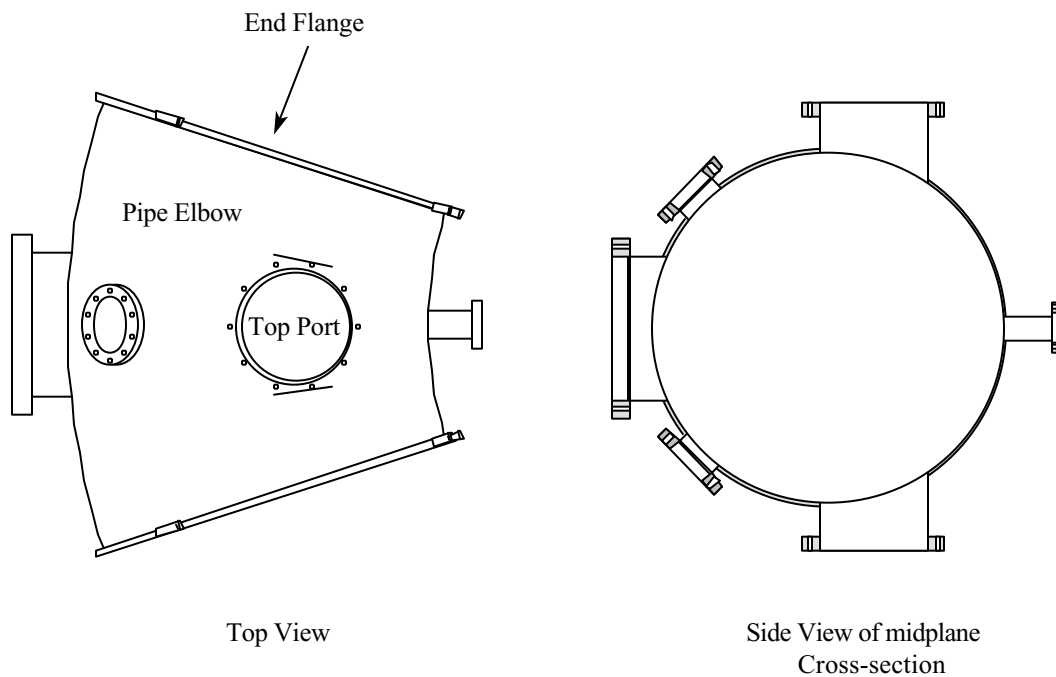
Top View   Side View of midplane
Cross-section

Fig 4.3 HBT-EP vacuum vessel segment

The ten chamber sections are joined by three different kinds of transition segments: insulating portions made of straight quartz tubing (18" diameter, 11 cm long), stainless steel

spool pieces and stainless steel flexible bellows sections. The peak electric field along the surface of each quartz portion is less than 45 V/cm with the fastest possible toroidal current startup. Quartz sections are compatible with ultra high vacuum requirements. They are transparent and thus provide access for visible radiation diagnostic measurements. They also are a preferred location of magnetic fluctuation diagnostics because fields rapidly penetrate non conductors. The spool pieces have small ports in them for diagnostics and limiter support. The bellows segments' flexibility absorbs manufacturing errors in the circumference of the vessel. All the transition pieces attach to the vacuum vessel with a double pumped O-ring seal. The region between the two O-rings is pumped on by a mechanical pump to reduce permeation through the inner O-ring.

The ten vacuum chamber segments are each supported both horizontally and vertically. From the inside of the vacuum vessel to the TF centering ring, a radial support beam opposes the vacuum centering force. From the cement base pad to the lower end of a vacuum chamber section, two vertical support beams (one on each side) oppose gravity. These supports are electrically insulated with G-10 fiber glass, they prevent relative motion between the segments themselves and between the segments and the support structure.

4.2.2 Pumps and controls

The HBT-EP vacuum chamber is evacuated with two cryo pumps with effective speeds of $\approx 2000(l/s)$, one turbo-molecular pump with a lower effective speed of $\approx 1000(l/s)$ and a series of back up mechanical pumps behind the turbo pump. Initial pump down procedures are started with a mechanical pump followed by the turbo pump bringing the machine to pressures

of $\approx 10^{-5} Torr$ before switching to the cryo pumps which lower the pressure to the ultra high vacuum levels ($\approx 10^{-8} Torr$) of HBT-EP's operation. The entire system of pumps, valves, gauges and other monitors (e.g. vacuum measurements, power measurements, air pressure etc.) is governed centrally by a vacuum system control panel located in the HBT-EP control room.

4.2.3 Vacuum conditioning

After the pump down of the vacuum chamber, the inside walls of the vessel must be conditioned, essentially water and oxygen have to be removed from the vacuum surfaces. The goal is to reach base pressures of $\leq 10^{-8} Torr$ with oxygen partial pressures of $\leq 10^{-12} Torr$. The two cleaning procedures are

a) Chamber bakeout

The baking of each vacuum chamber segment is done using two (top and bottom) of the forty separate insulating heating pads. The temperature of the vessel rises to a maximum of $110^{\circ} C$. It is regulated with ten separate controllers (one for each segment) and the total power available for the heating system is 20kW.

b) Glow discharge cleaning

This method of vacuum conditioning has been extensively practiced and its relative effects well examined [4,5]. Glow discharge cleaning involves filling the vacuum vessel with either deuterium or helium, in the tens of milliTorr range, and initiating a discharge in the chamber using an electrode that is inserted into the center of the vessel. Fig 4.4 below shows the setup built for HBT-EP.
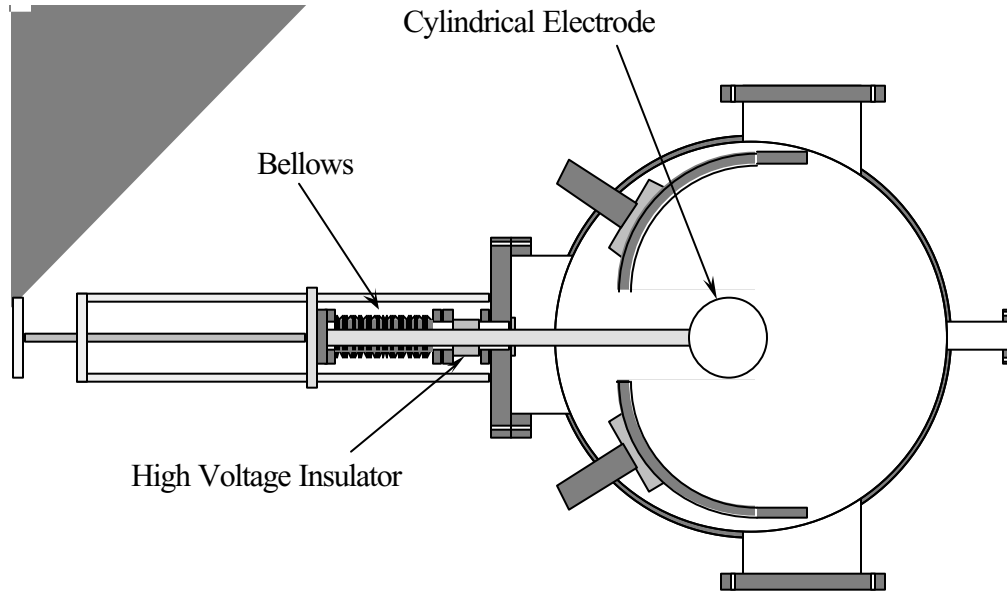
**Fig 4.4 Cross sectional view schematic of
the glow discharge cleaning electrode setup**

The electrode is DC biased positive with respect to the walls of the chamber. The vessel is filled with a neutral gas, such as deuterium, and when the breakdown occurs, an electrical circuit consisting of the electrode, the ionized gas and the chamber walls forms. The current in this closed circuit is an ion current and it is drawn to the walls. The ions then react with the adsorbed impurities in the walls and the impurities are driven off or simply knocked off the wall by striking ions. The power supply typically gives out 0.7A at 600V through a current limiting resistor of 250? with a Deuterium fill pressure of $10\,mTorr$.

4.3 Plasma-wall interactions

The principal purpose of magnetic confinement is the isolation of the hot plasma from the relatively cold surrounding first wall (s). However, some plasma always comes into contact with the first wall and other surfaces such as limiters and in HBT-EP's case the conducting wall inside the vacuum. These plasma facing components must be designed to withstand the plasma heat and particle fluxes and to minimize the impurities freed from the wall that will enter the

51

plasma and result in additional radiative energy losses. For HBT-EP and its relatively low temperatures and short pulse lengths, it is the second issue that is of concern.

4.3.1 HBT-EP's limiters

One common means of keeping plasmas from directly striking and hence interacting with the primary vacuum chamber wall is the use of a mechanical limiter. A limiter can consist of a metal ring in the poloidal direction or in the toroidal direction generally on the outside of the torus; or it may just be simple straight rail segments. Limiters must be capable of withstanding intense, sometimes localized, thermal fluxes without melting or cracking [6].

The size of the plasma in HBT-EP is determined by the location of the top, bottom and outside adjustable stainless steel rail limiters. These are located at two toroidal locations, see Fig 4.5. The inner edge of the plasma cannot be smaller than 75 cm since the stainless steel flanges on the vacuum vessel segments act as inner limiters.

The limiters are made from 3/8" thick type 316 stainless steel plates. The radial adjustable limiter has a range of motion of 10.8 cm which allows outer plasma radii from 103.1 cm to 113.9 cm. The vertical adjustable limiters have a range of motion of 4.6 cm which allows minor radii between 14.6 cm and 19.2 cm. In addition to the movable limiters
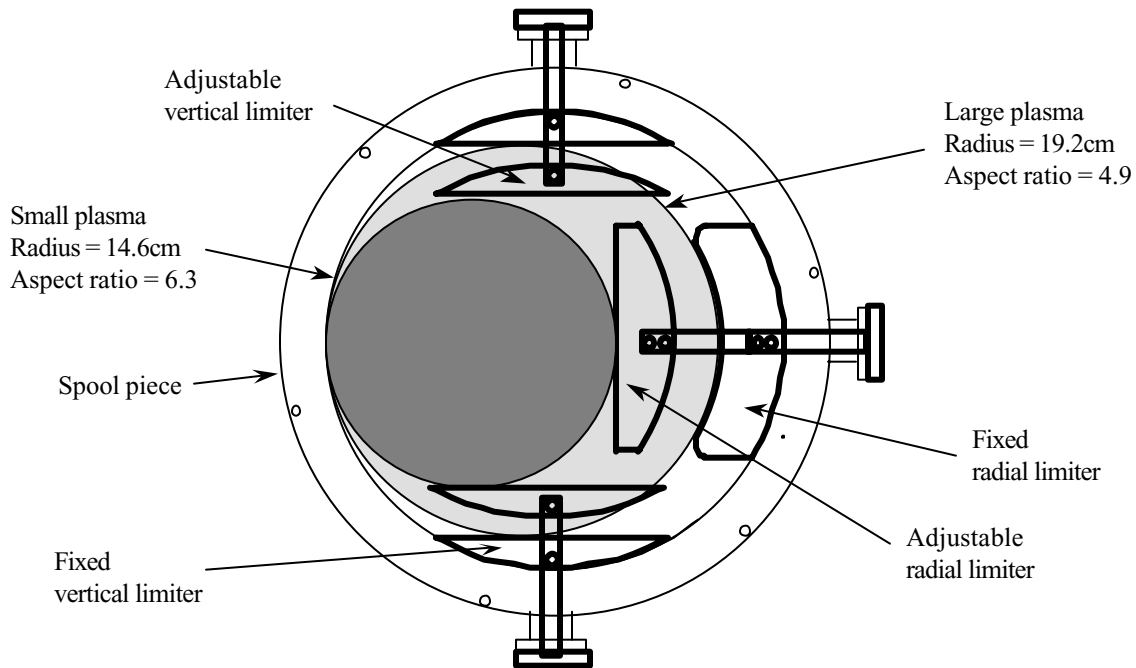
Fig 4.5 Cross sectional view of HBT-EP's adjustable limiters

at each location, there are fixed limiter blades to prevent current from flowing through unconfined plasma behind the limiters during small major radius operation. The movable limiter positioner assembly consists of stainless steel rods that attach to the blades on one end and to sealing Con-Flat flanges on the other end. Between the end Con-Flat flange and the machine port, a stainless steel welded bellows supported by four threaded rods with jack screws (not shown in Fig 4.5) accurately place the limiter blade at the desired radial position. The range of plasma aspect ratios achievable is A=4.9-6.3.

4.3.2 HBT-EP's conducting walls

The HBT-EP approach to the study of passive and active control of MHD instabilities begins with internally mounted and electrically isolated modular adjustable conducting walls. These segments or *shells* are made of 0.013 m thick spun aluminum with a 0.002" thick

coating of pure Nickel, which is selected as a plasma facing material due to its low sputtering yield. The major radius of the wall is $R_0 = 92cm$, and its minor radius is $b = 16cm$, which puts it 1 cm away from HBT-EP's small plasmas configuration $(R_0 = 92cm, a = 15cm)$. The wall consists of 20 separate sections, two in each of the ten large vacuum chamber portions. They are individually mounted at the end of a movable positioner. The conducting plates are located, at a $\pm45°$ angle to the mid plane of the torus, see fig 4.6.
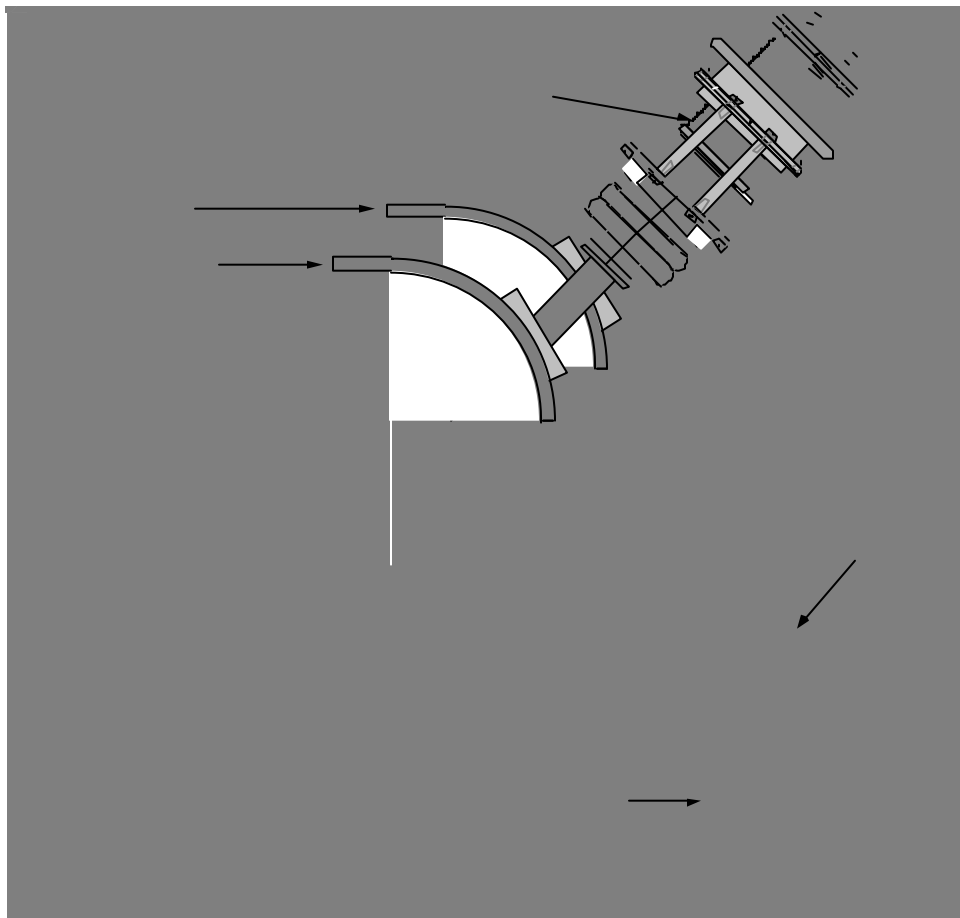
When the limiters are fully inserted, the plasma minor radius a is fixed and the conducting wall position can be varied over a range of 0.01-0.09m from the surface of the plasma ($1.07 \leq b/a \leq 1.52$, where b is the radial distance of the conducting plates from the

plasma center), see Fig 4.7. The conducting wall segments are shaped with circular cross sectional plasmas in mind, they cover up to 78% of the plasma surface when all 20 of them are fully inserted.

Shells retracted: <b>/a = 1.52   Shells inserted: b/a = 1.07
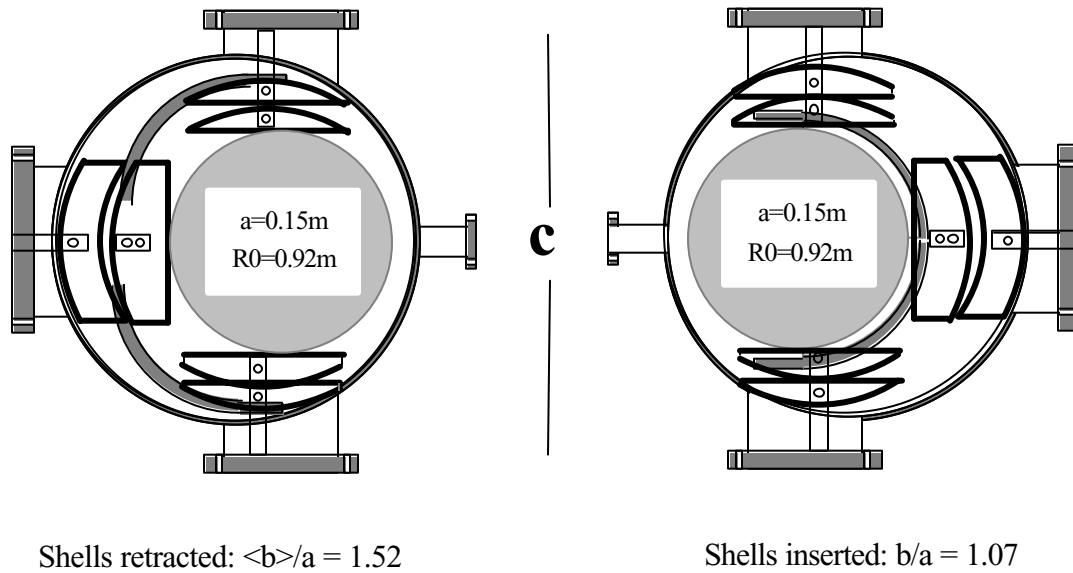
Fig 4.7 HBT-EP's vacuum chamber cross section showing poloidal limiters and conducting shells in the inserted and retracted configurations

References

[1] D. Gates, Ph.D. thesis, Columbia University, 1993.

[2] D.R. Robinson et al., Plasma Physics and Controlled Nuclear Fusion Research **1986** IAEA, Kyoto (1986).

[3] M.K.V. Sankar et al., J. Fusion Energy **12** 303 (1993).

[4] H.F. Dylla, J. Vac. Sci. Tech. A **6** 1276 (1988).

[5] F. Waelbroeck et al., , J. Vac. Sci. Tech. A **2** 1521 (1984).

[6] R. Gross, *Fusion Energy*, (John Wiley & Sons, NY 1984).

Chapter 5
DIAGNOSTICS AND OPERATION

In order to understand plasma behavior in HBT-EP, the following pertinent parameters must be determined: total plasma current, plasma position, loop voltage, magnetic field fluctuations, total radiated power and soft x-ray flux. The principal diagnostics used for these measurements are briefly described in this chapter. A layout showing the various locations of the different diagnostic systems is displayed in Fig 4.1.

5.1 Magnetic diagnostics

Magnetic diagnostics are essential in understanding the MHD equilibrium and stability properties of tokamak plasmas. HBT-EP uses 136 magnetic probes. Some are inside the vacuum and some outside. Some are used for local measurements and others are used for global plasma measurements.

a) <u>Internal magnetic probe</u>

The magnetic field inside the plasma can be detected using 13 vertical field coils and 2 radial field coils supported on a G-10 form encased in a thin stainless steel jacket. This multi-point magnetic probe is movable. It can be used to measure the field outside the plasma or it can be fully inserted into the core of the plasma to calibrate other diagnostics. This is done only when required since introducing the probe into the plasma deteriorates the performance of the discharge.

b) <u>Global magnetic diagnostics</u>

The most basic measurements are that of plasma current and position. These are made using Rogowski coils located around quartz sections of the vacuum chamber.

Total plasma current, I_P, is measured using a compensated Rogowski coil. This is a multiple turn solenoid that completely encloses the current to be measured. The transient plasma current generates a poloidal magnetic field which induces the detected voltage V. For a uniformly wound solenoid with N turns per unit length and a diameter d, V is given by the expression

$$V = N\pi \frac{d^2}{4} \mu_0 \frac{dI_P}{dt} \tag{5.1}$$

A passive RC circuit integrates this voltage, from which the total plasma current, I_P, is deduced. A complete poloidal loop around the plasma would be sensitive to changes in the toroidal magnetic field, therefore one end of the solenoid is connected back through its center thus providing compensation for unwanted fluxes [1].

The same device can be used to measure plasma position by modifying the winding pitch of the basic solenoid. The Rogowski coil is wound with a density of turns proportional to the sine or cosine of the poloidal angle θ around the coil. Horizontal bulk plasma motion is then detected by the $\cos\theta$ coil and vertical motion is given by the $\sin\theta$ coil. The signal from these coils is a function of the offset of the center of the current centroid from the geometric center of the sine or cosine coil [2]. For example, the expression for the cosine coil is given by

$$V_{coil} = f(R_{plasma} - R_{coil})I_P + K_{VF}I_{VF} + K_{OH}I_{OH} + corrections \tag{5.2}$$

The function f is taken to be a polynomial of order three. The K's are measured from vacuum shots. The corrections come from image currents that flow in conductors near the plasma, such

as the vacuum chamber and the conducting wall segments. The coils are calibrated on the tokamak using the plasma position measured by the internal magnetic probe as a reference.

Rogowski coils with winding densities varying like $\cos(m\theta)$ or $\sin(m\theta)$ where $m > 1$ (e.g. $m=2$ or $m=3$) are used to observe MHD mode structures and their modification prior to disruptions. The fluctuations we seek to measure are characterized by poloidal magnetic field perturbations having a mode structure defined by [3]

$$\tilde{B}_\theta = \mathrm{A}_{nm} \exp\left[i\omega_{nm}t - m\theta - n\Phi\right] \qquad (5.3)$$

where $\tilde{B}_\theta$ is the oscillating component of B_θ, θ and Φ are the poloidal and toroidal angles, m and n are integers referred to as mode numbers and ω_{nm} is the angular frequency of the (m,n) mode in the frame of reference of the plasma. Therefore, the measurements concern the external azimuthal variation of the poloidal magnetic field B_θ, related to current-dependent plasma surface disturbances. B_θ, can be expressed as a sum of poloidal Fourier harmonics and a perturbation expansion can be done in the lab frame. The first order perturbed field, $\tilde{B}_\theta$, can be considered proportional to $\cos\theta$ or $\sin\theta$ and the mth order term to the mth order Fourier harmonic and so on. The $\cos(m\theta)$ and $\sin(m\theta)$ coils instantaneously perform the Fourier analysis of the signals. The output from such coils (e.g. $\cos 2\theta$ or $\sin 3\theta$ of HBT-EP) is directly proportional to the time derivative of the required Fourier component. Only the m number of the mode is determined this way. For the n number, a phase comparison is done on two toroidally separated coils.

The plasma current produces a toroidal loop voltage as per Ohm's law. This single turn voltage is measured using flux loops (single-turn pick-up coils) that are wound toroidally near the inner and outer radii of the vacuum vessel.

Figure 5.1 below illustrates typical measurements obtained on HBT-EP from the above described coils. In particular, the total plasma current, the plasma position, the loop voltage and signals from two Fourier-analyzing Rogowski coils sensitive to $m=2$ and $m=3$ magnetic fluctuations are shown respectively in parts (a), (b), (c), (d) and (e) of the plot.

c) <u>Shell mounted probes</u>

Shell mounted probes are small magnetic pick-up coils attached on the conducting wall. 72 coils are distributed at the central poloidal region on both sides of four HBT-EP conducting wall segments. Eddy-current measurements are made by calculating the difference between the magnetic fields located on opposite sides of a conducting wall section. By assuming that the thickness of the conducting plate is small compared with the scale lengths of the variation of the eddy currents, $\vec{\kappa}$, Ampere's law can be written as

$$\mu_0 \vec{\kappa} = \hat{n} \times \left[\vec{\tilde{B}}_{out} - \vec{\tilde{B}}_{in} \right] \tag{5.4}$$

where $\vec{\tilde{\kappa}}$ is the fluctuating surface current, $\hat{n}$ is the unit vector normal to the surface of the shells and $(\vec{\tilde{B}}_{out}, \vec{\tilde{B}}_{in})$ refer to the magnetic fields on the outer and plasma-facing side of the conducting wall. A more elaborate description of these magnetic coils is in [4].

d) <u>External point probes</u>

These are small external pick-up windings consisting of a poloidal array of 15 (B_θ, B_r) coils and a toroidal array of 5 (B_θ, B_r) coils. All are mounted on plastic supports just outside the five quartz vacuum chamber segments. This location allows the measurement of high resonance magnetic field oscillations.
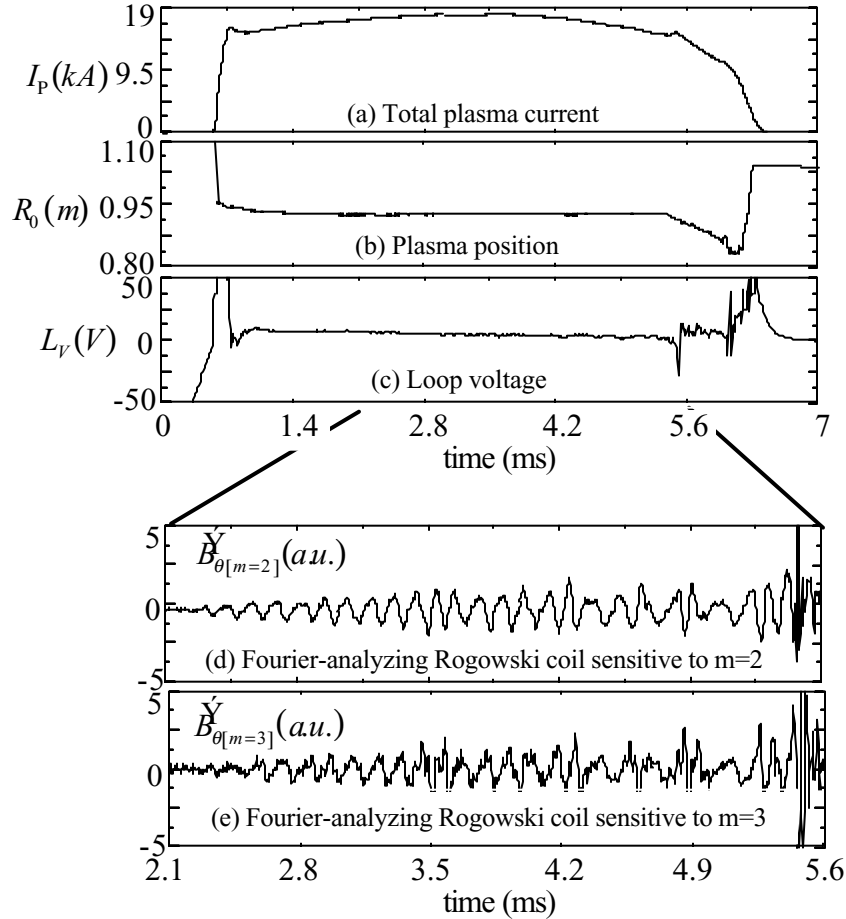
Fig 5.1 Typical HBT-EP measurements from shot # 8817

5.2 Soft x-ray array

The soft x-ray flux is a function of electron temperature, electron density and effective charge. Therefore, soft x-ray diagnostics are sensitive to changes in these quantities and their small fluctuations can be easily detected. This together with magnetic perturbations diagnostics allows the study of MHD instabilities.

One of the more useful diagnostics on HBT-EP is the sixteen channel array of XUV photodiodes. This array provides profile information and probes the plasma internally. A sketch of its mechanical assembly inside the vacuum chamber port is shown in Fig 5.2.
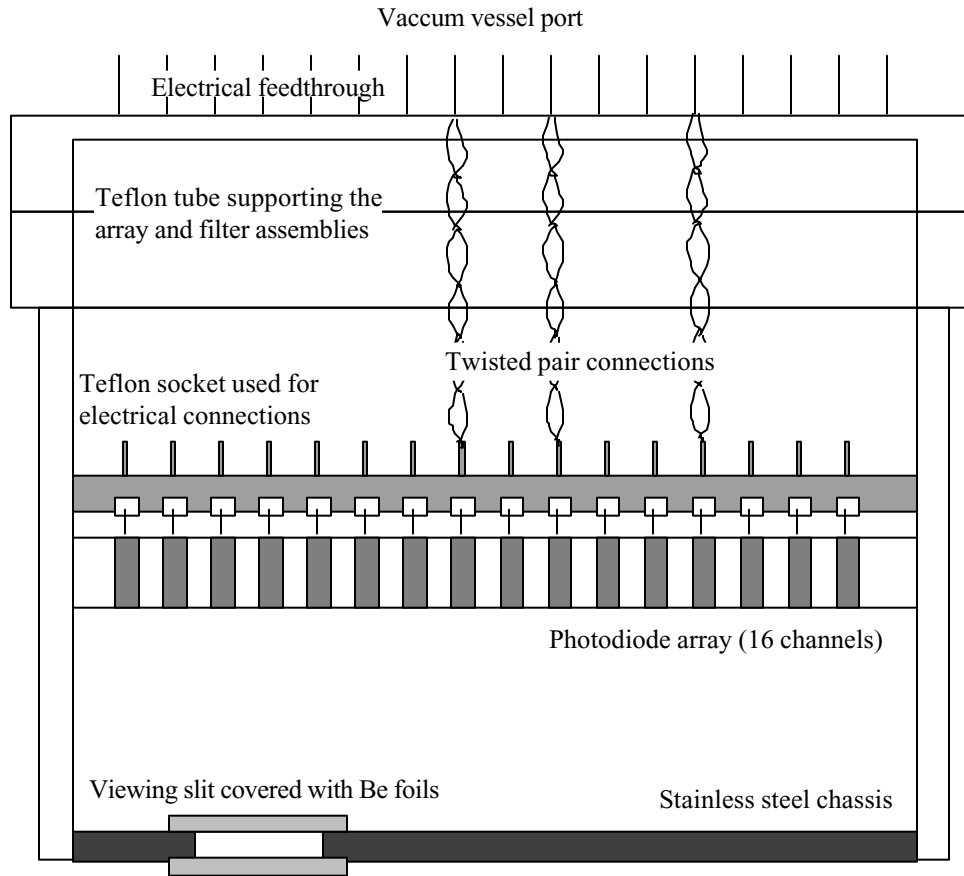
61

Fig 5.2 Sketch of the 16 channel photodiode array assembly inside the vacuum chamber port

5.2.1 The detectors

The detectors are silicon p-n junction XUV photodiodes with energy range from $7eV$ to $6000eV$ manufactured by International Radiation Detector (IRD). Each of the devices has an active area of $10\ mm^2\ (2\ mm \times 5\ mm)$, a low capacitance on the order of $100\ pF$ and a response time of $0.5\mu s$. The diodes are mounted on a ceramic chip package $(5.3\ cm \times 2\ cm)$ in series with a $0.5\ mm$ separation between them thus creating an array of sixteen channels. Each channel is electrically connected to two opposing pins on the package.

The four corner pins on the chip represent the anode (connected to ground in our case). The IRD part number for this chip is AXUV-16LO.

When a photodiode is exposed to photons of energy greater than 1.12 eV (wavelength less than 1100nm), electron-hole pairs (*carriers*) are created. These photogenerated carriers are only separated by the p-n junction electric field and a current proportional to the number of electron-hole pairs created can flow through an external circuit. Unlike common p-n junction diodes, these devices do not have a doped dead-region and have zero surface recombination resulting in very high quantum efficiencies (electrons seen by external circuit per incident photon) predicted in most of the XUV region by the theoretical expression $E_{ph}/3.63$ where E_{ph} is photon energy in electron-volts (eV) [5]. Also, these XUV diodes are internal photoelectric devices and hence are not very sensitive to minute vacuum system contaminants that usually affect conventional XUV detectors based on the external photoelectric effect. Therefore, the photodiode array can be placed inside the vacuum and operated without added difficulties.

5.2.2 Beryllium filter and photodiode response

In order to *blind* the devices to visible light and limit their energy range to that of soft x-rays, a Beryllium filter assembly is used between the detectors and the plasma. The assembly consists of a stainless steel round chassis with a slit in it and Beryllium foils. The chassis was machined at Columbia and later sent to ACF Metals where two Beryllium foils, each 200 *nm* thick, were epoxied on the stainless steel.

63

The Beryllium foils, fragile as they are, were reinforced with an ultra-thin non-obstructing mesh. The two foils were mounted in series on each side of the chassis thus bringing the effective thickness of the Beryllium between the plasma and the detectors to 400 nm. Figure 5.3 shows the calculated transmission for a Beryllium film, 400 nm thick, for photons in the X-UV and soft x-ray range. This was carried out using data tabulated by Henke *et al* [6] for thin film transmissions calculated from photoabsorption cross sections. Beryllium bulk density was taken to be 1.85 $g \cdot cm^{-3}$ and Beryllium $K_{edge} = 111eV$ was assumed. The filter assembly makes the devices most sensitive to plasma soft x-ray emission radiation in the energy range from 40 eV to 111eV.
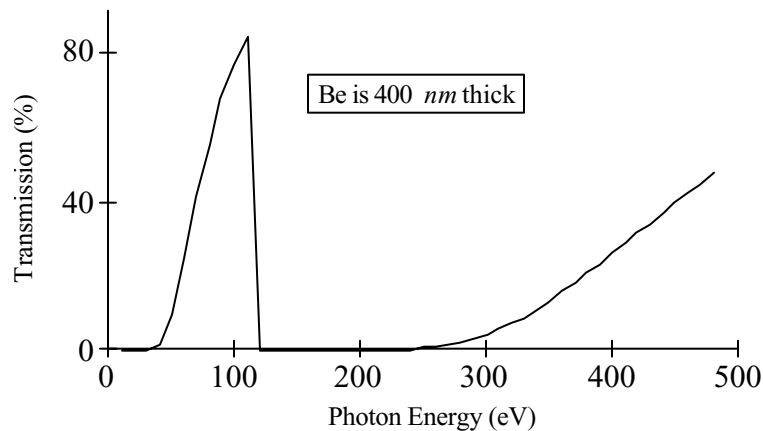

Fig 5.3 Beryllium transmission response to photon energy

Relative response of the photodiodes viewing the plasma through the Beryllium filter to different temperatures has also been calculated. Only bremsstrahlung and recombination radiation were taken into account in the computation. A theoretical quantum efficiency of one electron-hole pair per 3.63 eV photons was assumed for the photodiodes. The calculated Beryllium transmission was then combined with the theoretical quantum efficiency to get the

response of the detector-filter assembly. Figure 5.4 shows the resulting photo current for detectors using 400 nm and 600 nm thick Beryllium as a function of plasma temperature.
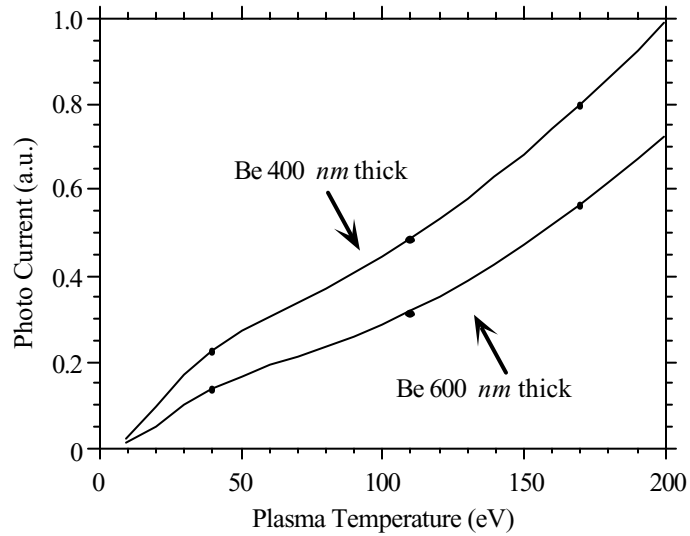

Fig 5.4 Relative response of photodiodes with various thickness Beryllium filters vs plasma temperature

5.2.3 Trans-impedance amplifier

The photodiodes are connected to a vacuum electrical feedthrough with Kaptan insulated wire in a twisted pair configuration to avoid magnetic pick-up (see sketch in Fig 5.2). The signals are then amplified using sixteen trans-impedance amplifiers. A Burr Brown chip

operational amplifier OPA 627 AM (metal package) is employed as the main component of the circuit. It is chosen because of its high bandwidth (10 MHz) and its low input bias current (20 nA). Each amplifier channel is powered individually with a ± 12 V power supply for better isolation and to avoid ground loops. All sixteen of these trans-impedance amplifiers have the same gain. The amplified signals are then sampled at the rate of 100 KHz using Aurora A-12 digitizers. Figure 5.5 shows a diagram of the circuit.
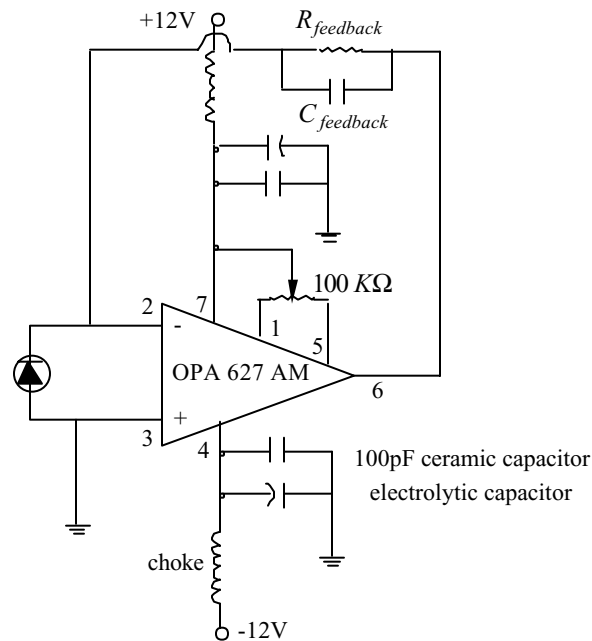

Fig 5.5 Circuit diagram of the trans-impedance amplifier used with the photodiodes

5.2.4 Calibration

The detector-slit assembly was bench calibrated (without the Beryllium filter) using a monochromatic DC light source to exactly map out the span of each channel. The specific

66

viewing chords of each detector in the poloidal plane are shown below in Fig 5.6. The differences due to varying solid angles extents from channel to channel were calculated and taken into account in our signal interpretation.
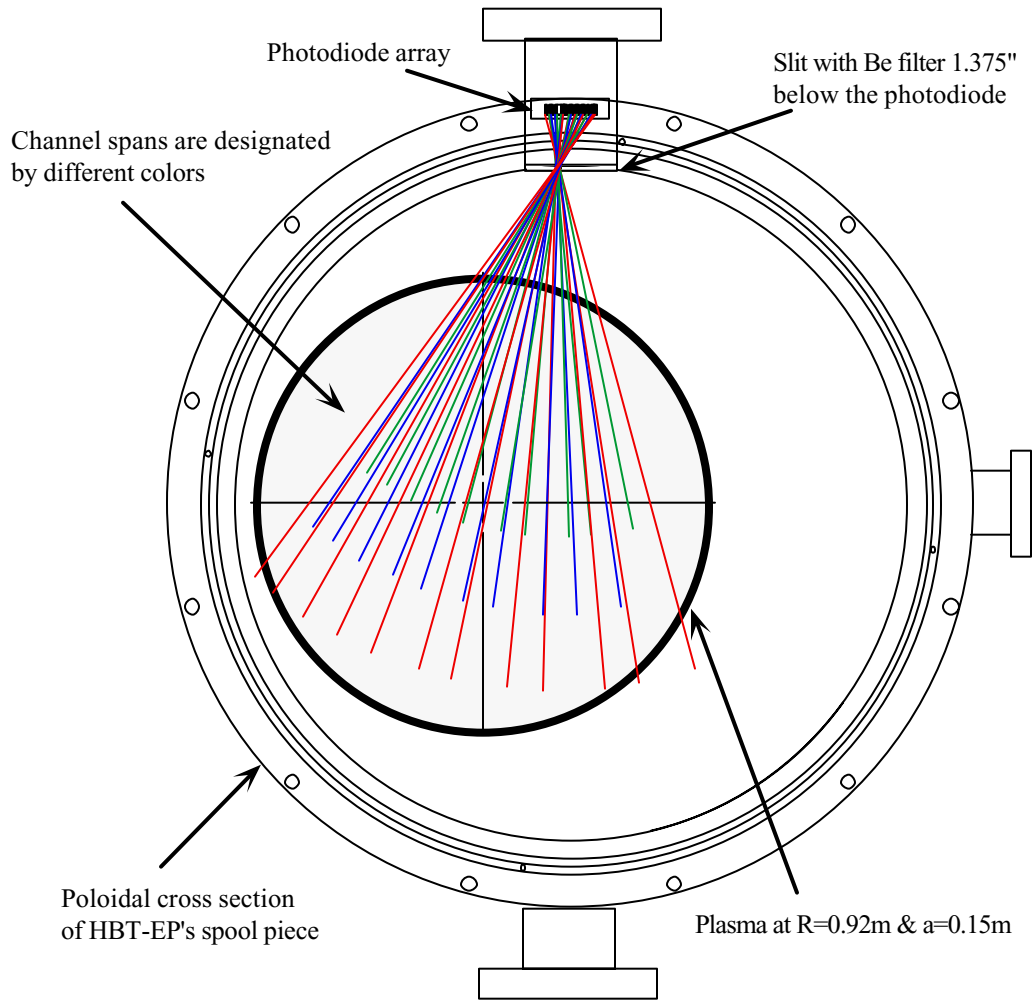
Photodiode array

Slit with Be filter 1.375" below the photodiode

Channel spans are designated by different colors

Poloidal cross section of HBT-EP's spool piece

Plasma at R=0.92m & a=0.15m

Fig 5.6 Soft x-ray array channel map out

5.2.5 Typical measurements

The signals, once multiplied by the appropriate calibration constants, are plotted either in contour form or just as raw data. Figure 5.7 displays typical soft x-ray plots. In part (a) two

chord integrated signals are overlaid. The blue trace is from a plasma-edge detecting channel and the trace in red is from a plasma-core viewing channel that exhibits periodic thermal crashes, known as sawteeth. In part (b), all sixteen channels are used to form a contour plot.
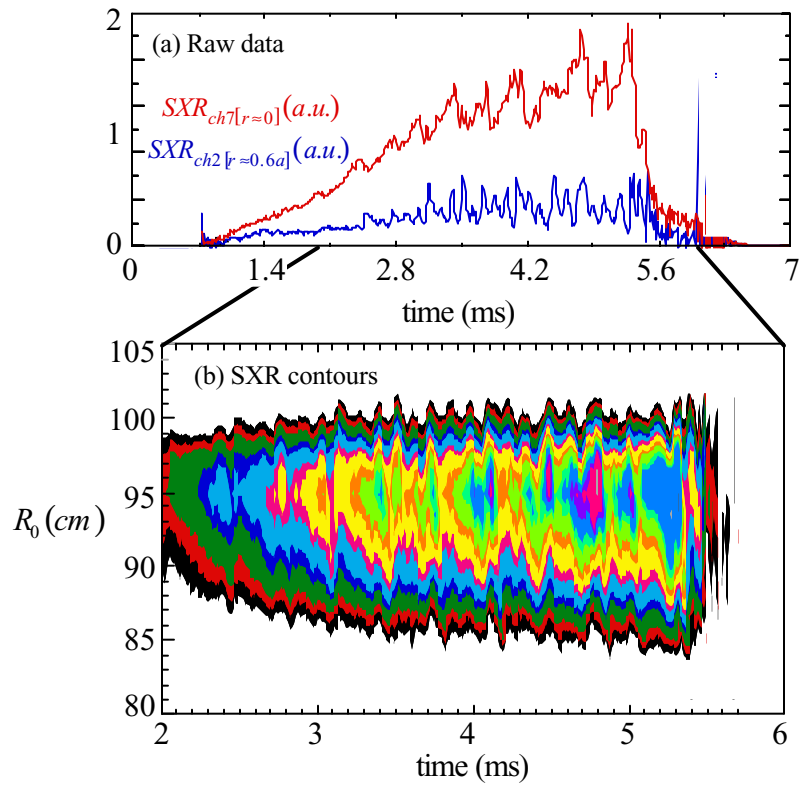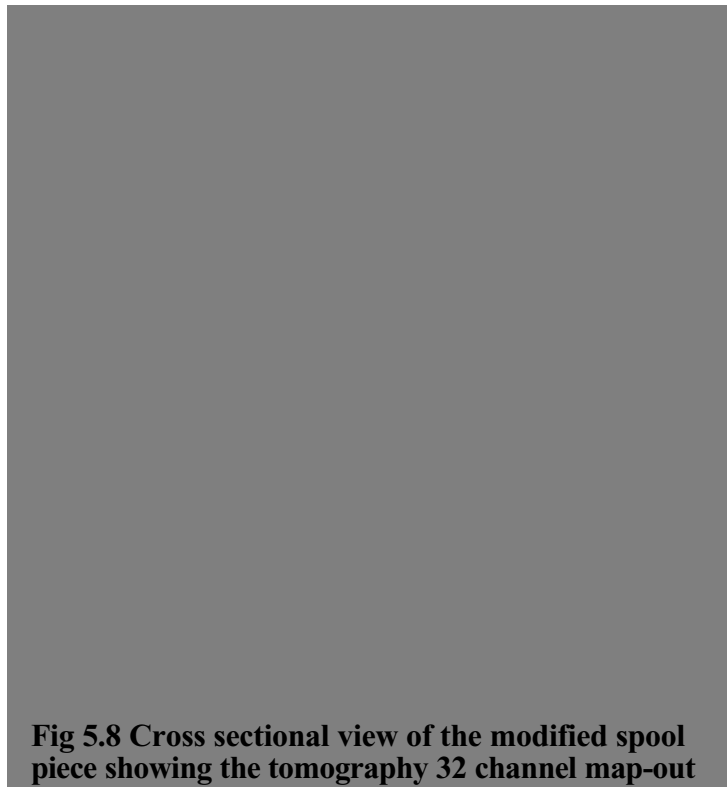

Fig 5.7 Soft x-ray signals for a sawtoothing discharge

5.3 Tomography

A 32 channel tomography system is employed to study MHD mode structures on HBT-EP. The system is installed on a modified spool piece section of the vacuum chamber, see Fig 5.8. In its initial phase, eight vertical and eight horizontal channels were utilized to detect both visible and UV light emission from the plasma. Later, the set-up was modified to view the soft x-ray radiation profile. The new system consists of 32 collimated channels of soft x-ray sensitive photodiodes placed on each port making these devices uniformly distributed in both r and θ directions. The photodiodes are coated with a specially designed thin film filter made of 100nm Zr, 7.5nm Ti and 75nm C [7,8]. The thin film filter cuts visible and UV spectrum. The signals, similar to those detected by the soft x-ray array, are in $10's$ to $100's$ of μA.

Fig 5.8 Cross sectional view of the modified spool piece showing the tomography 32 channel map-out

5.4 Broad band radiometer

An X-UV100 photodiode manufactured by UDT Sensors Inc. is used to measure total radiated power from the plasma over a broad spectral band. The detector is a silicon p-n junction device developed for use in the X-UV spectral range which covers photons with energies between 6 eV and 12 KeV. The photodiode has a high stable quantum efficiency which is predicted by the simple expression $E_{ph}/3.63eV$ [9]. The active area of the device is $1\ cm^2$. Just like the soft x-ray array, the photodiode has no external bias applied across it (thus eliminating leakage currents) and the current detected is amplified through a trans-impedance amplifier similar to the ones used by the array channels (see section 5.2.3). Fig 5.9 shows a diagram of the detector assembly on a spool piece of the vacuum chamber.
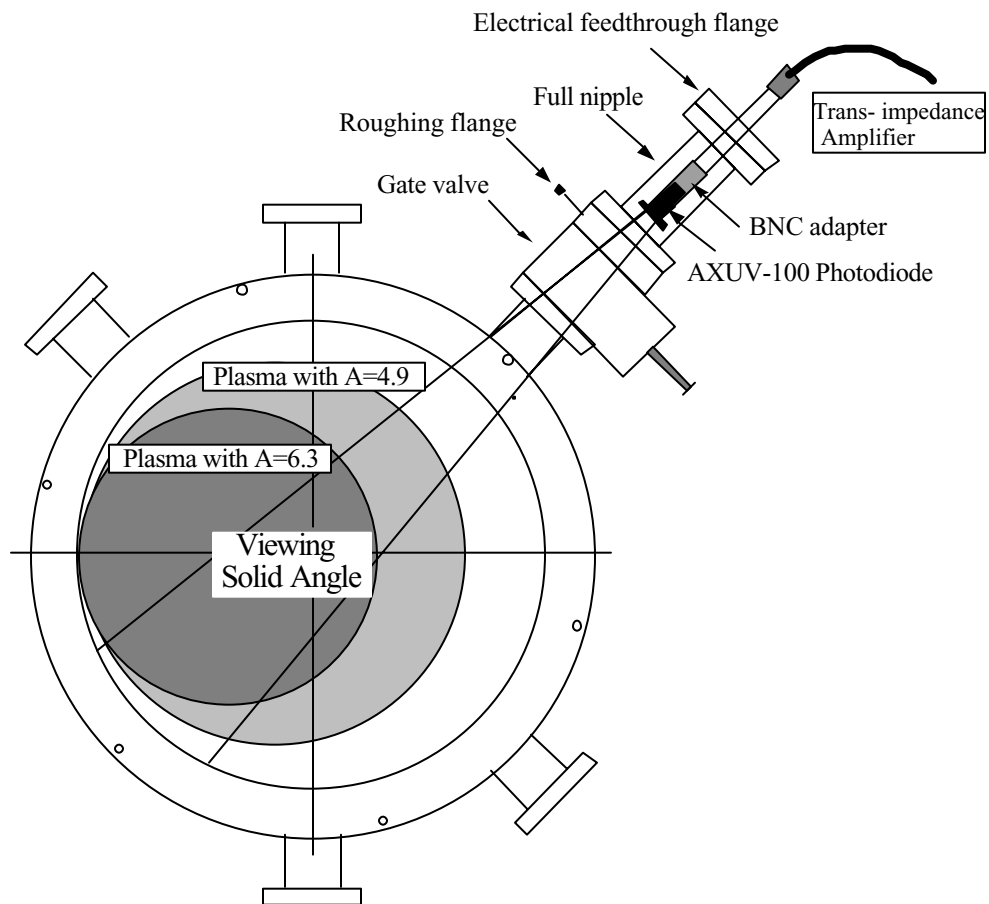

Fig 5.9 Cross section view of spool piece with Radiometer assembly

5.5 Data acquisition

Signals from the various diagnostics (e.g. magnetic probes, Rogowski coils, flux loops, soft x-ray diodes) are recorded by digitizers located in CAMAC crates mounted in shielded racks located around the experiment. Once the data is digitized, it is read over a fiber optic serial data-link, which is connected to a MicroVax 4000-200 where the information is stored on disk. A schematic of the setup is shown in Fig 5.10.
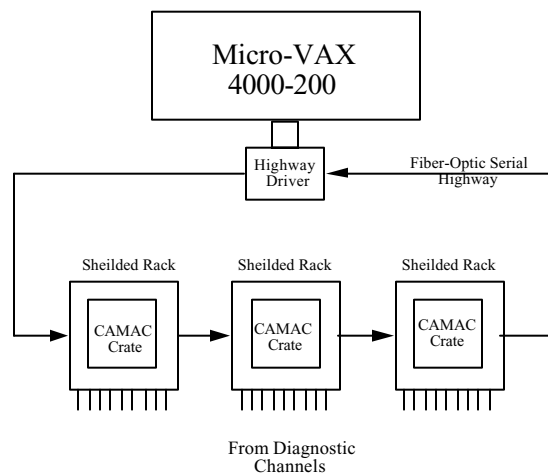

Fig 5.10 Schematic of HBT-EP's data acquisition system

The database management software used is the MDS system developed at MIT. Raw data, calibration data and processed data are all written and stored in different levels of the HBT-EP database.

5.6 Plasma formation

Different types or classes of discharges can be obtained on HBT-EP. The controls that can be adjusted are the gas source, the bank voltages, the electron source (or e-gun) and the limiters.

Prior to discharge, capacitor bank voltages are selected to achieve the preferred plasma current ramp rates and the desired total plasma current levels along with the appropriate field strengths. Pulsed piezo-electric puff valves used together or individually provide the required gas source. Ionization is initiated from a pulse of electrons emitted from an electron gun inserted near the edge of the plasma.
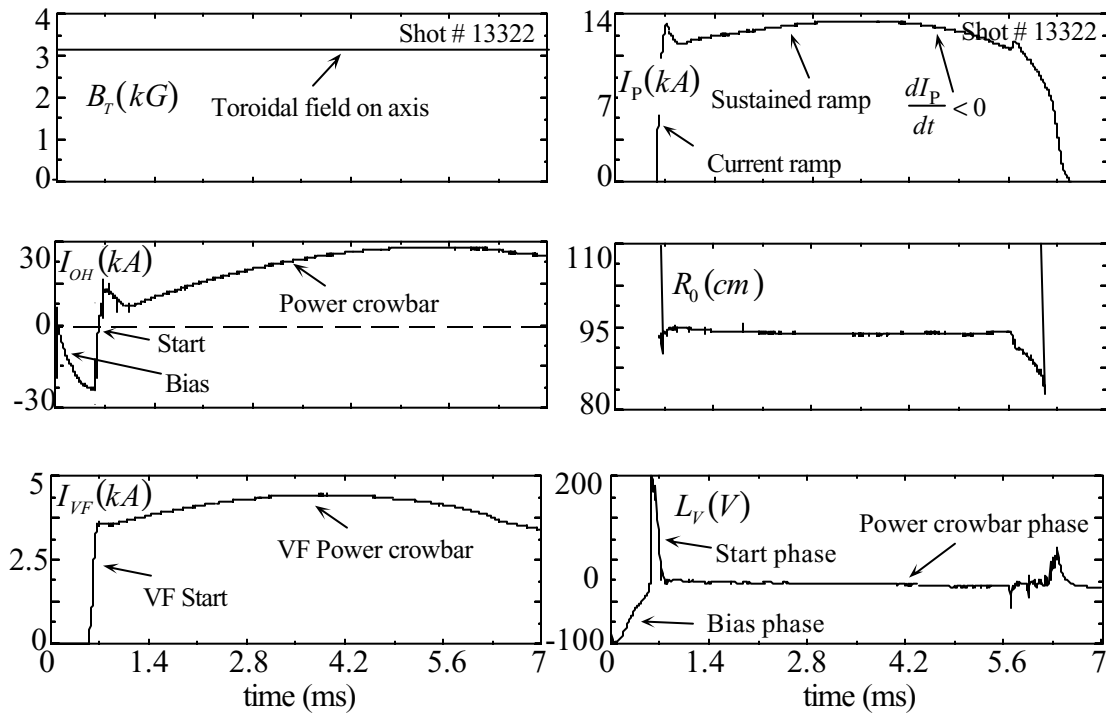

Fig 5.11 Typical waveforms for a shot on HBT-EP

Figure 5.11 above shows representative waveforms from an HBT-EP discharge. The shot sequence begins with the firing of the toroidal field bank at $t \approx -117$ ms. Then, the gas is puffed at $t \approx -60$ ms, before the start of the shot. Next, the electron gun is pulsed during the bias phase of the ohmic heating. This is followed by firing the ionizing "start" portion of the ohmic heating bank. The "bias" bank voltage is adjusted so that the peak bias current equals the

peak start current. The plasma current is then sustained at the required value by the "power crowbar" bank.

The "start" vertical field bank fires at approximately the same time as the start ohmic heating bank. The vertical field "power crowbar" is fired when the start bank reaches peak current. The voltages on the vertical field bank (start and power crowbar) are chosen so that the plasma center, as measured by the cosine coil, is in the experimentally desired location.

Figure 5.12 below shows another achievable start-up on HBT-EP, different than the one displayed in Fig 5.11. The discharge initiation sequence is similar to the one explained above, but its characteristics and the plasma formation are distinct. By "dialing" in different values of bank voltages and slightly altering the gas puff, sharper current ramp rates can be obtained giving rise to a different category of plasmas.
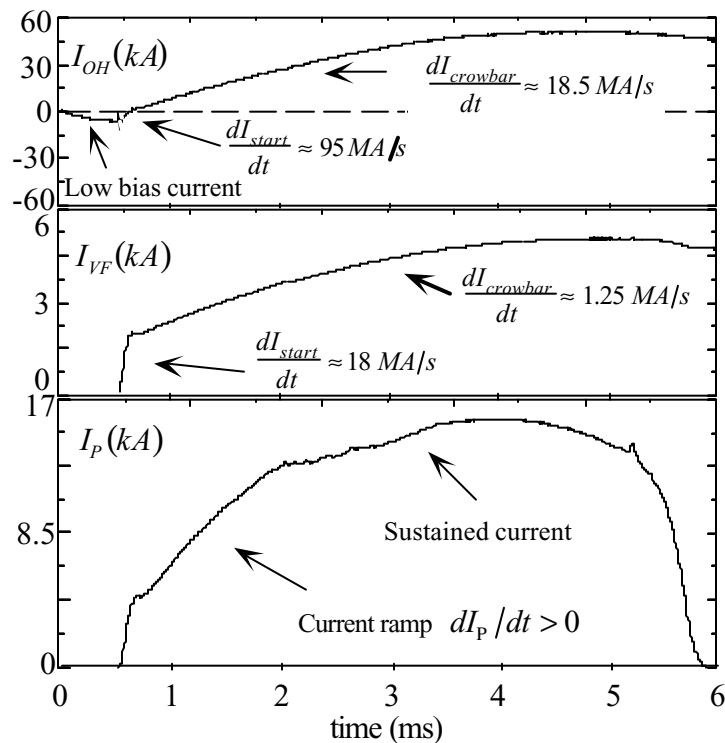

Fig 5.12 Formation sequence for a current-ramp discharge

In Fig 5.11, after the rapid formation, a slight positive ramp rate was maintained, as evident on the total current trace, followed by a negative ramp down phase. In Fig 5.12, the plasma current was slowly ramped to its peak value, after which a ramp down phase occurred due to exhausted volt-seconds on the power crowbar.

It is important to note that during these various ramp phases ($dI_\mathrm{P}/dt > 0$, $dI_\mathrm{P}/dt < 0$) and depending on how slow or sharp they are, the current profile of the plasma is being modified. Broad profiles with high edge currents are expected in the slow current-ramp discharges. Slightly more peaked profiles are presumed in the weak $dI_\mathrm{P}/dt > 0$ phase of the rapid formation discharges. Peaked profiles with high edge-gradients are expected in the ramp down phase $dI_\mathrm{P}/dt < 0$ of the discharges.

5.7 Current profiles

In order to better illustrate current profile changes during the different ramp periods in the discharge's lifetime, a simulation of expected profiles was done. The model adopted cylindrical geometry and the plasma was considered a solid. Constant density, $T_e = T_i = T$ and Spitzer [10] plasma resistivity were assumed. The magnetic diffusion equation together with the heat equation for plasmas with parameters similar to the HBT-EP ones were solved simultaneously and a current profile $J(r)$ was calculated. The equations used were

$$\frac{\partial T}{\partial t} = \chi \frac{1}{r} \frac{\partial}{\partial r}\left(r \frac{\partial T}{\partial r} \right) + \frac{\eta J^2}{3nk} \tag{5.5}$$

$$\frac{\partial \psi}{\partial t} = \frac{\eta}{\mu_0} \frac{1}{r} \frac{\partial}{\partial r}\left(r \frac{\partial \psi}{\partial r} \right) \tag{5.6}$$

where η is the plasma resistivity, χ is the electron thermal conductivity and ψ is a flux function such that $\vec{B} = B_0 \hat{z} + \hat{z} \times \nabla \psi$. Boundary and initial conditions were chosen consistent with HBT-EP plasmas.

Figure 5.13 shows an overlay of various profiles obtained from two plasmas comparable to the ones in figures 5.11 and 5.12. These profiles correspond to the three types of current ramps obtained in the two classes of discharges examined. The times considered are chosen to best represent the ramp phases, to have matching values of total plasma current and to capture the start of the disruptive instabilities when applicable.

The trace in black is a broad profile with high edge currents. It is as expected in slow-current ramp discharges (see Fig 5.12). Ideal MHD theory (see ch 2) predicts the appearance of $m=2$ external kinks in conjunction with these profiles [11]. The remaining traces are from a discharge rapidly formed and similar to the one shown in Fig 5.11. The trace in blue represents the modest positive $dI_P/dt > 0$ phase of the discharge right after the rapid formation. It also has a broad profile. It is, however, slightly more peaked and with lower edge-currents than the profile corresponding to the slow current ramp plasma. Finally, the trace in red corresponds to the negative current ramp phase $dI_P/dt < 0$. It has a peaked profile with steep edge gradients. This type of profile is susceptible to tearing mode instabilities [12].
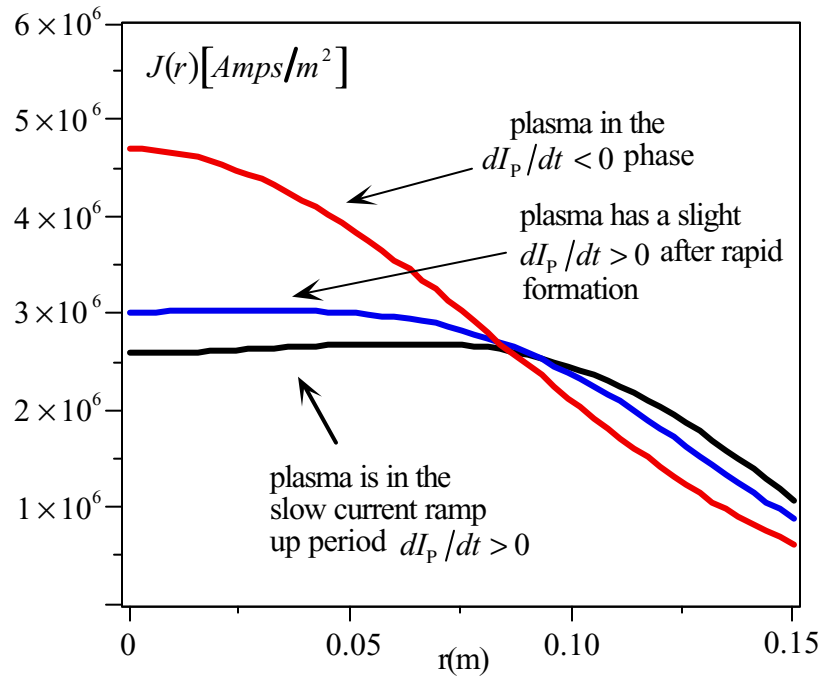
**Fig 5.13 Current profiles for three different
current ramp phases from two distinct plasmas**

In summary various plasmas can be obtained on HBT-EP, depending on the formation

technique. The different plasmas are created with diverse current ramp rates and can go through

distinct ramp phases ($dI_P/dt > 0$ and $dI_P/dt < 0$) during their lifetime. Three of these current

ramp phases occurring on two types of discharges are singled out and their corresponding

profiles described. The two classes of plasma have the common feature of being susceptible to

disruptive instabilities. The disruptions can happen in any of the three ramp phases depending on

the position of the conducting wall around the surface of the plasma. This implies that disruptions

can be observed in conjunction with the three current profiles specified above. The next chapter

focuses on understanding these different disruptions and compares their mechanisms.

References

[1] I.H. Hutchinson, *Principles of Plasma Diagnostics* (Cambridge University press, NY 1987).

[2] H.Y. Che et al., Rev. Sci. Inst. **59** 1057 (1988).

[3] Equipe TFR, Nuc. Fusion **18** 647 (1978).

[4] A. Garofalo, Ph.D. thesis, Columbia University, 1996.

[5] R. Korde et al., SPIE (x-ray instrumentation) **1140** 126 (1989).

[6] B.L. Henke et al., At. Data Nuc. Data Tables **54** 181 (1993).

[7] Q. Xiao and G.A. Navratil, Rev. Sci. Inst. **67** 3334 (1996).

[8] Q. Xiao, Ph.D. thesis, Columbia University, 1997.

[9] L. Canfield et al., Applied Optics **28** 3940 (1989).

[10] F. Chen, *Introduction to Plasma Physics and Controlled Fusion* (Plenum press, NY 1984).

[11] J. Friedberg, *Ideal Magnetohydrodynamics* (Plenum press, NY 1987).

[12] J.C. Hosea et al., Plasma Physics and Controlled Nuclear Fusion Research **1970** IAEA, Madison (1970).

Chapter 6
WALL STABILIZATION STUDIES

The main objective of this work is to study the effectiveness of the segmented conducting shell in avoiding or suppressing external kink driven disruptions and β-limiting disruptions both of which occur on HBT-EP. With the preceding chapters as background and this objective as a goal, a series of experiments were carried out. Using circular cross section plasmas, the conducting wall elements were withdrawn to their outermost position where $\langle b \rangle / a = 1.52$ (b is the radial position of the conducting shells and a is the minor radius of the plasma), and discharges were initiated to oberve the thresholds of the disruptive instabilities. Then moving the shells systematically and incrementally closer to the surface of the plasma up to where $b/a = 1.07$, while maintaining a constant plasma cross section and position using the poloidal limiters, the influence of the HBT-EP close fitting segemented wall on disruptions was documented. What follows are the details and results.

6.1 "Current-ramp" vs "Rapid formation" discharges

In shell studies on HBT-EP, two types of discharges were chosen to illustrate conducting wall effects on the stability and disruptivity of the plasma. The "knobs" used to initiate these two different plasmas were limited compared to other tokamaks. As mentioned in earlier chapters, capacitor banks determine startup and field strength, puff valves control densities and limiters position the plasmas. Therefore by tweaking these settings the two classes of discharges were obtained. The idea was to make one type of plasmas that will exhibit external kink disruptions and another type of plasmas that will illustrate β-limiting disruptions.

In the first category, designated "current-ramp" discharges, plasmas were formed with a prescribed gradual current ramp of $dI_P/dt \approx 6 \, MA/s$ to induce a broad current profile with enhanced edge currents known to excite external kinks. The other type of plasmas, designated "rapid formation" discharges, were created using a fast startup with a $dI_P/dt \approx 100 \, MA/s$ followed by a much slower current ramp to produce plasmas with more peaked profiles and higher values of β_N near the disruptive limit. Figure 6.1 below shows a comparison of the two types of discharges. The MHD parameters plotted indicate a declining edge safety factor, q^*, and lower values of β_N for the current ramp plasmas where as the rapid formation plasmas have a constant q^* and increased β_N.
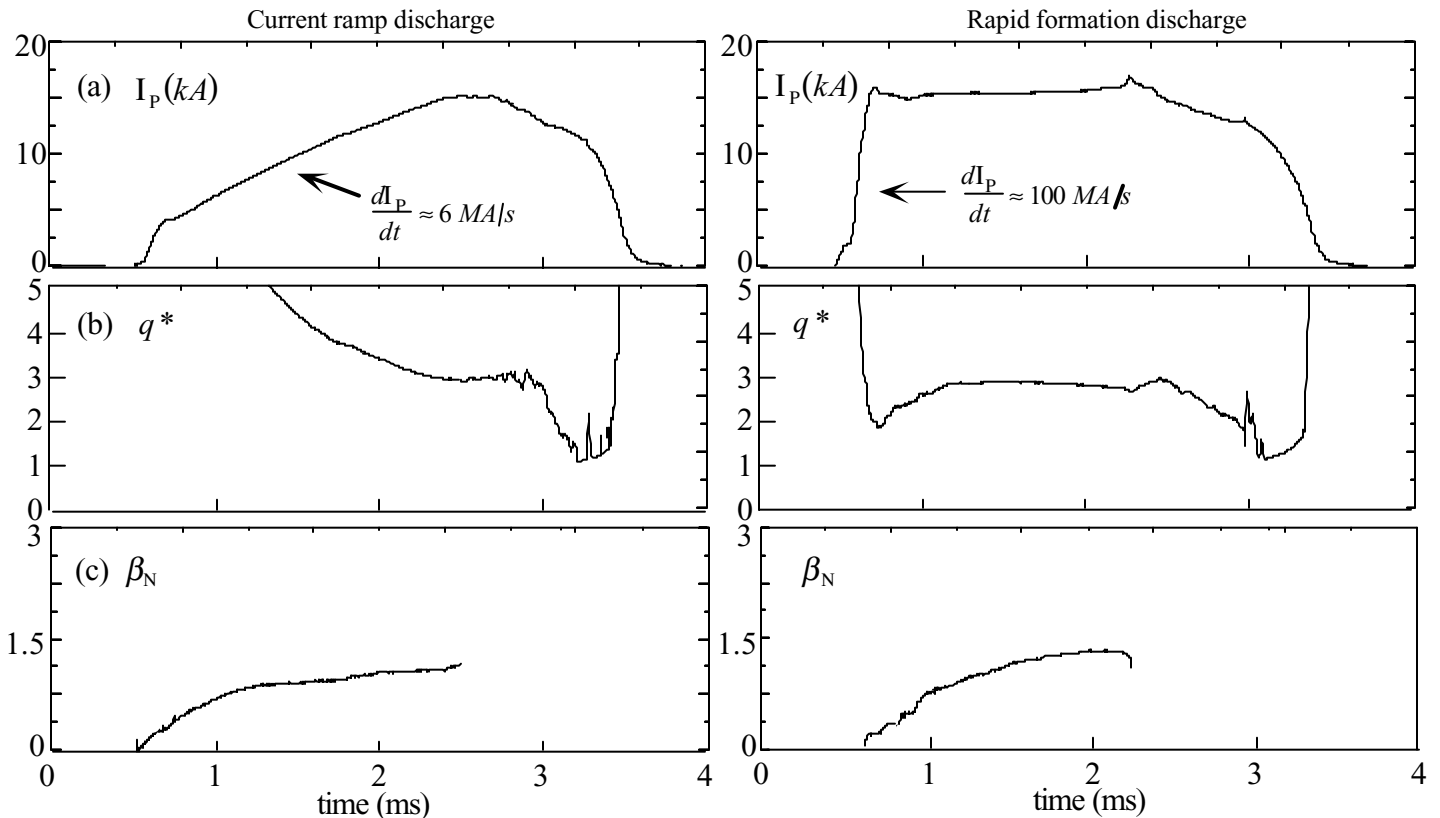

Fig 6.1 Comparison of "current ramp" and "rapid formation" discharges showing (a) total plasma current, (b) cylindrical safety factor and (c) normalized beta

6.2 External kink disruptions

Ideal MHD theory predicts that plasmas possessing finite current or current gradients at the plasma boundary, such as the above current ramp discharges, are susceptible to external kink instabilities in the absence of a conducting wall independent of the value of β [1,2]. These instabilities are predicted to occur below integer values of the cylindrical edge safety factor $q*$ for circular cross section plasmas.

In order to examine the shell effects on these discharges, two similarly prepared plasmas with identical parameters were obtained, one with the conducting shells fully inserted (b/a=1.07) and the other with the shells fully retracted (b/a=1.52). Figure 6.2 compares the time evolution of the total plasma current, the plasma position, the loop voltage, the total radiated power and the edge safety factor for the two discharges.
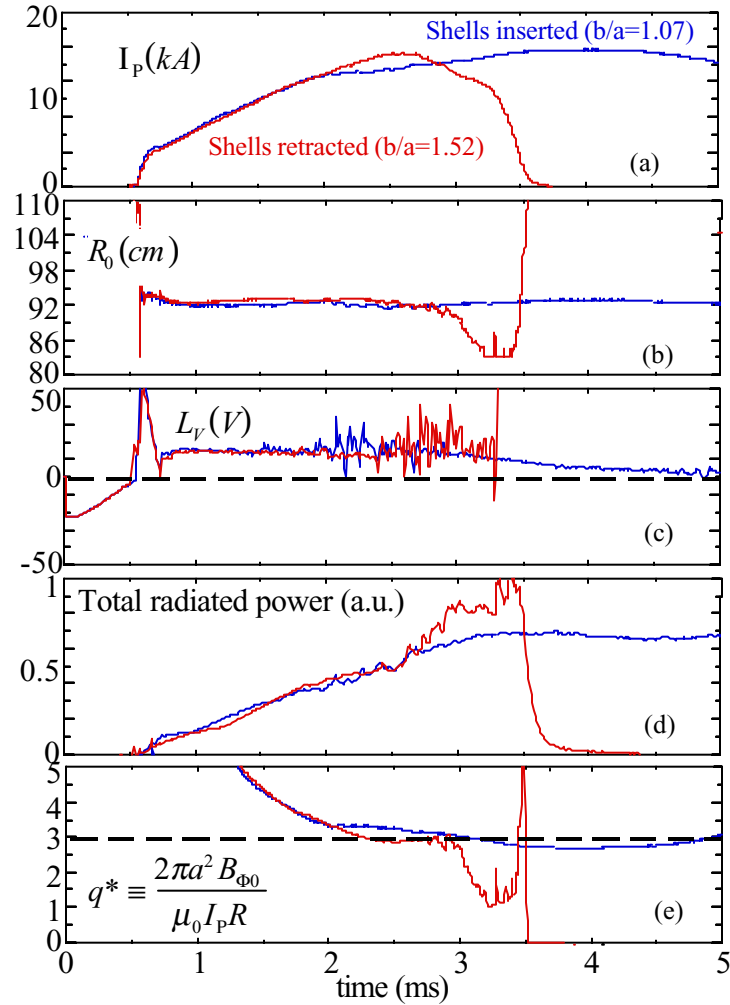
**Fig 6.2 Comparison of current-ramp discharges
with shells inserted and shells retracted**

The traces in red are with the shells retracted and the plasma disrupts as edge-q drops

below 3. The blue traces are for the discharge with the shells fully inserted, $q*$ also drops below

3 but no disruption occurs. The plasmas in both cases were maintained as close as possible as

evident from their global parameters which develop exactly the same way until the time of

disruption of the discharge with the shells retracted. The toroidal field was held constant, so that

the ramping plasma current produced a cylindrical edge safety factor, $q*$, that decreased with

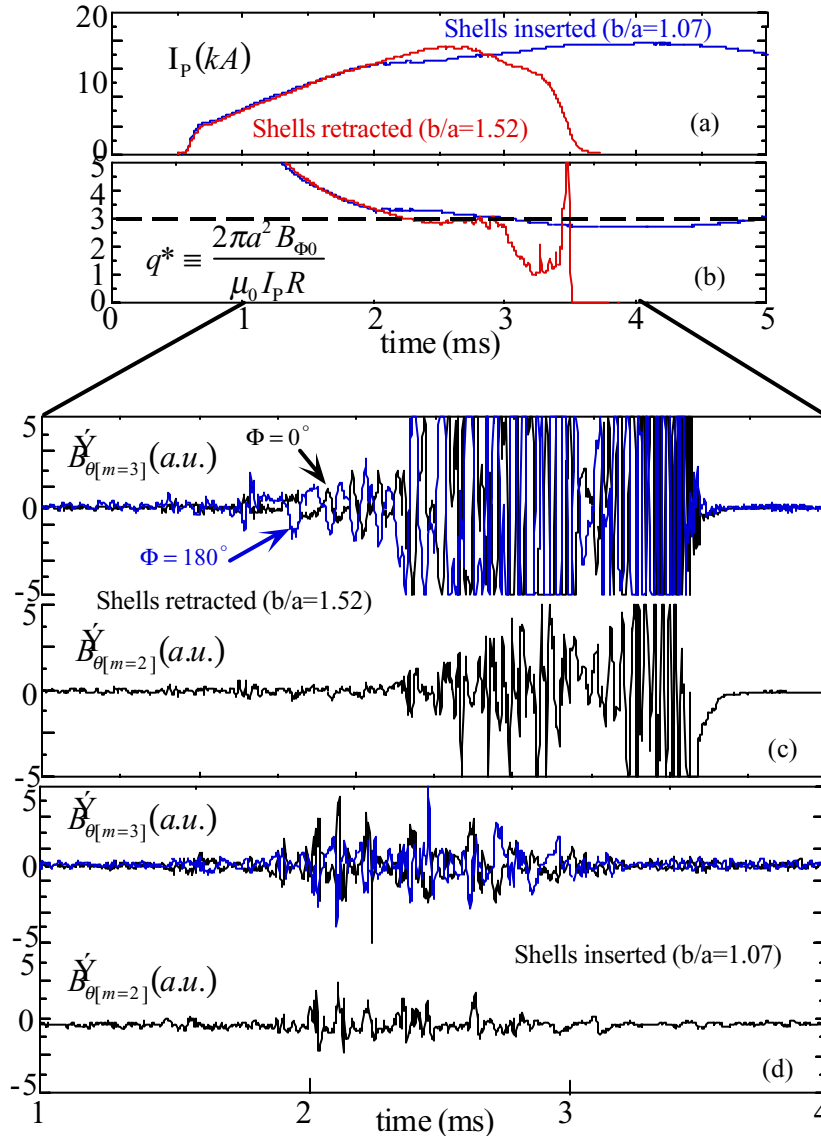time. The MHD activities of both discharges are examined next.

Fig 6.3 Comparison of MHD precursors in current-ramp discharges for both shells retracted and insrted cases

In Fig 6.3 a comparison of current-ramp discharges with shells inserted and shells retracted showing total plasma current, cylindrical safety factor and magnetic activity sensitive to $m=3$ and $m=2$ fluctuations is displayed. In the discharge formed with shells retracted, magnetic fluctuations appeared at $t=1.7\ ms$ with $q^* \approx 3.6$. Data from Fourier-anlyzing Rogowski coils toroidally separated by 180° and Minorv loops indicate that the structure of the perturbation is predominantly poloidal mode number $m=3$ and toroidal mode number $n=1$. Initially, the

instability grew with a charateristic growth time of $\gamma^{-1} \approx 350\,\mu s$ and the fluctuations sustained an amplitude of $\delta B_\theta / B_\theta (r = a) \approx 0.7\%$ for $500\,\mu s$. Then as $q*$ dropped below 3 at $t=2.4\ ms$, the mode amplitude doubled in about $30\,\mu s$, the current ramp was stopped, the plasma deteriorated and a disruption followed.

For the plasma formed with the shells fully inserted, the begining of the sequence was the same. As $q*$ decreased, similar magnetic fluctuations started to appear at $q* \approx 3.5$. Again, the instability had an *m/n=3/1* magnetic structure and was accompanied by bursts of *m=2* activity. These internal fluctuations eventually reduced the current ramp rate, possibly due to increased plasma resistivity during the decline of $q*$ from 3.6 to 3. As $q*$ dropped below 3, the magnetic perturbations disappeared, the discharge became quiescent and lasted without disrupting, in sharp contrast to the disruptive plasma with the shells retracted.

An important point here is that for both shell positions (*b/a*=1.52 and *b/a*=1.07), the discharges initially had magnetic fluctuations with *q=m/n* resonant surfaces internal to the plasma. As the resonant surface of the mode exited the plasma, the fluctuations either caused the termination of the discharge, in the shells retracted case, or were eliminated in the shells inserted case. Figure 6.4 illustrates this idea by showing the decreasing edge-safety factor and the

following ratio $\left| \dfrac{\tilde{B}_{\theta\,[m/n=3/1]}}{\tilde{B}_{\theta\,[m/n=2/1]}} \right|_{r=a}$ which selects the dominant fluctuating component (*m/n=3/1* or

m/n=2/1) of the disruptive mode. If the dominant component has its resonant surface (*q=m/n*) outside the plasma as measured by $q*$ then the mode is external otherwise it is internal.
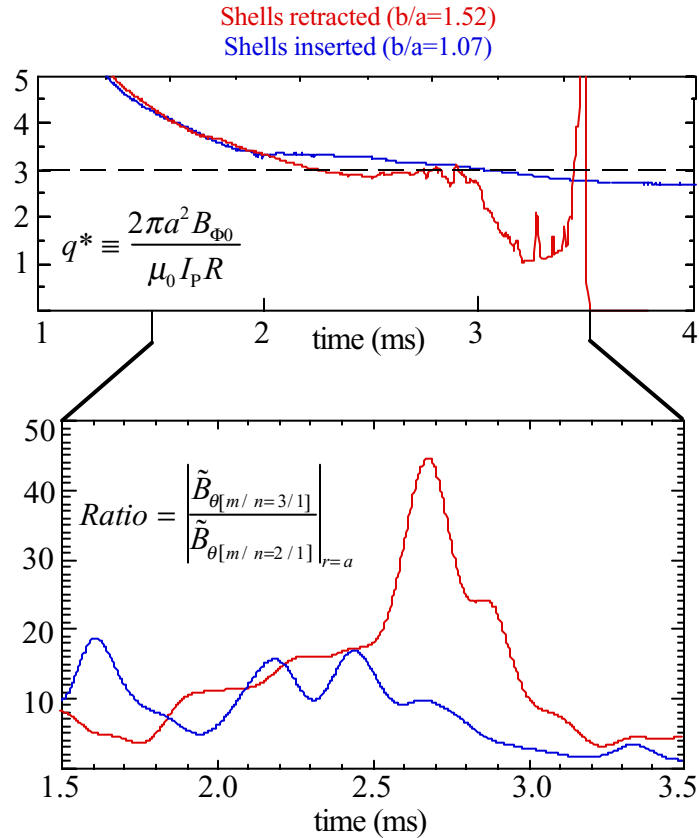
83

Fig 6.4 Plasmas with the shells retracted disrupt because of external modes

For the discharge with the shells retracted, at $t=2.4ms$ and as $q*$ gets below 3 indicating that the resonant $q=3/1$ surface is exiting the plasma, the fluctuations from the 3/1 component of the instability become much stronger (approximately 45 times larger in magnitude at $t=2.7ms$) than the fluctuations from the 2/1 component prior to the disruption. This implies that the disruptive mode is a predominantly external mode. As for the discharge with the shells inserted, at $t=3.1ms$ and as $q*$ is crossing 3 also indiacting that the $q=3/1$ surface is exiting the plasma, the magnitude of the fluctuations from the 3/1 component of the mode becomes much lower (approximately 10 times lower) than when the q=3/1 rational surface was inside the

84

plasma. This indicates that the external component of the mode is getting eliminated, *stabilized*, by the presence of the shells.

These examples demonstrate the effectiveness of the segmented shells in stabilizing a kink instability with the *q=m/n* resonant surface (in this case 3/1) outside the plasma. The disruption caused by the external kink was prevented by the close-fitting shells. The internal tearing instabilities present with the wall stabilized discharges will be addressed later in section 6.4 in this chapter.

6.3 β-limiting disruptions

In the current-ramp plasmas, weak ohmic heating because of the slow ramps resulted in low values of $\beta_N \approx 1$ at the time of disruption for the shells retracted dischages. However, fast formation plasmas are rapidly ionized relative to the ohmic heating soak through and have more peaked profiles where most of the current is deposited in the center early on. These rapid formation discharges heat up quickly and reach higher values of $\beta_N > 1.4$.

In order to examine the shell effects on these type of dicharges, two similarly prepared plasmas were obtained with the shell position being the only difference between them. Figure 6.5 compares the time evolution of the total plasma current, the plasma position, the loop voltage, the total radiated power and the rising β_N. The traces in black are for the plasma with the shells fully retracted (*b/a* =1.52) and the traces in red are for the plasma with the shells fully inserted (*b/a*=1.07). The discharges develop exactly the same way, their global parameters progress at the same rate and are kept as close as possible until $t\tilde{}2.2$ms, when the plasma with

the shells retracted disrupts as its β_N is reaching the ideal stability limit of 1.5. The plasma with

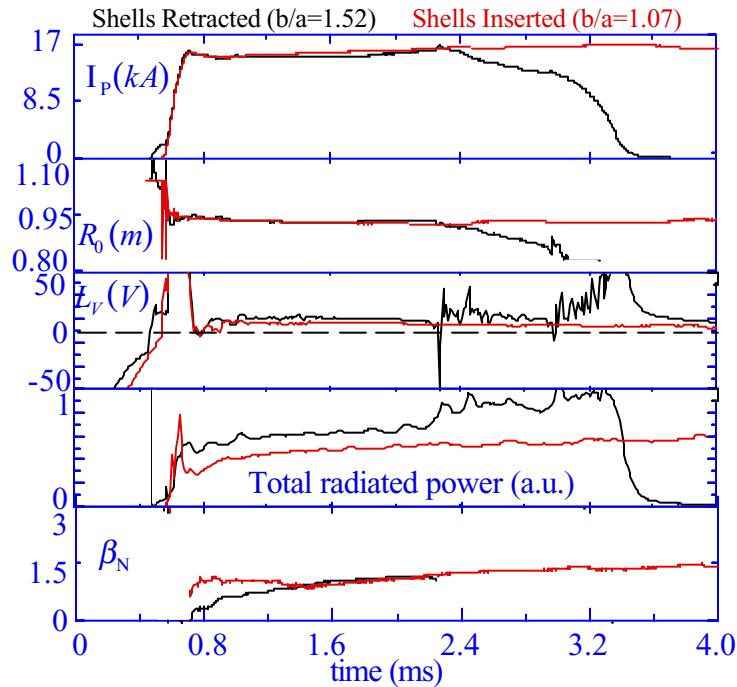the shells inserted proceeds without any disruptions

**Fig 6.5 Comparison of rapid formation discharges
with the shells inserted and shells retracted**

even as the value of its β_N continues to rise with the modestly increasing plasma current. The

point is that with the shells retracted a β-limiting disruption terminates the plasma where as for

the shells inserted this disruption is avoided.

The confirmation that these rapidly-formed discharges are indeed disrupting because the

value of their β_N is exceeding the stability limit can be seen in Fig 6.6 where β_N is plotted vs

$q(a)$. Shown here are the ideal MHD stability boundaries for discharges with HBT-EP

parameters calculated[4] using the PEST-II [5] code. The first important observation is that the

n=1 external kink stability boundary with the HBT-EP shells fully retracted is similar to the limit

with conducting wall at infinity. This implies that from an ideal MHD standpoint, fully retracting the shells in HBT-EP is like removing them altogether. The second noticeable item is that with the shells inserted, the predicted achievable β_N is double the value of the shells retracted case around $q(a)=2.7$. Finally, three data points from the rapid formation series of discharges are overlayed on the plot.
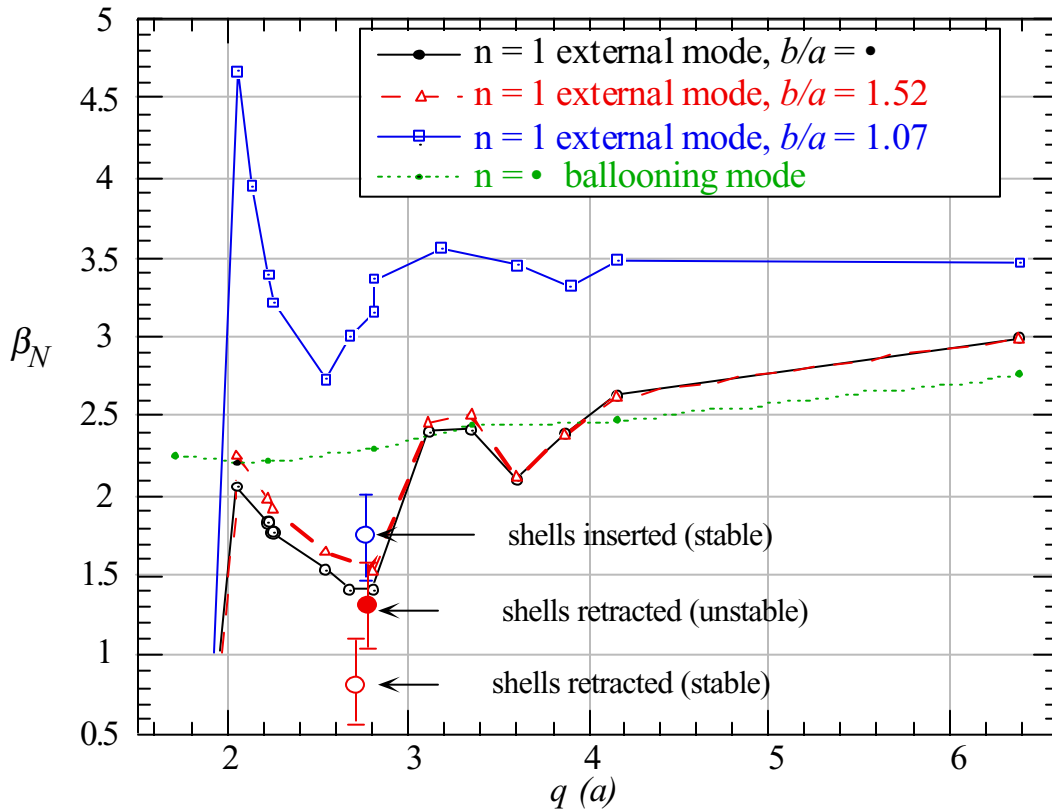

Fig 6.6 Ideal MHD modeling predicts instability to n=1 external kink at $\beta_N \approx 1.5$ with the shells retracted

The plasma at $(q(a), \beta_N) \approx (2.7, 0.9)$ is stable even with the shells retracted (the value of β_N is below the stability limit). The plasma at $(q(a), \beta_N) \approx (2.8, 1.9)$ is stable with the shells inserted but the value of its β_N is below the predicted one since with ohmic power as the only source of plasma heating, the upper n=1 stability boundary cannot be probed. The plasma at

$(q(a), \beta_N) \approx (2.8, 1.5)$ (which is the disruptive discharge shown in Fig 6.5) is unstable at $\beta_N \approx 1.5$, the value of the calculated stability boundary for the shells retracted HBT-EP plasmas.

Next, the disruption mechanism is examined for this unstable discharge and a comparison with the shells inserted case is presented. In Fig 6.7, the characteristics of a β-limiting disruption and the sequence of its occurrence are examined for a shells retracted case. The total plasma current and β_N are shown in part (a) as a reminder. Two soft x-ray (SXR) channels one central and one at 2/3 the minor radius are shown in part (b). In part (c), the soft x-ray contours over 1/3 of the diameter of the plasma are displayed. Finally in parts (d) and (e), signals from the Fourier-anlyzing Rogowski coils are also shown. The termination process appears to be initiated from within the plasma core, where a sawtooth-like collapse in the center of the sxr profile.
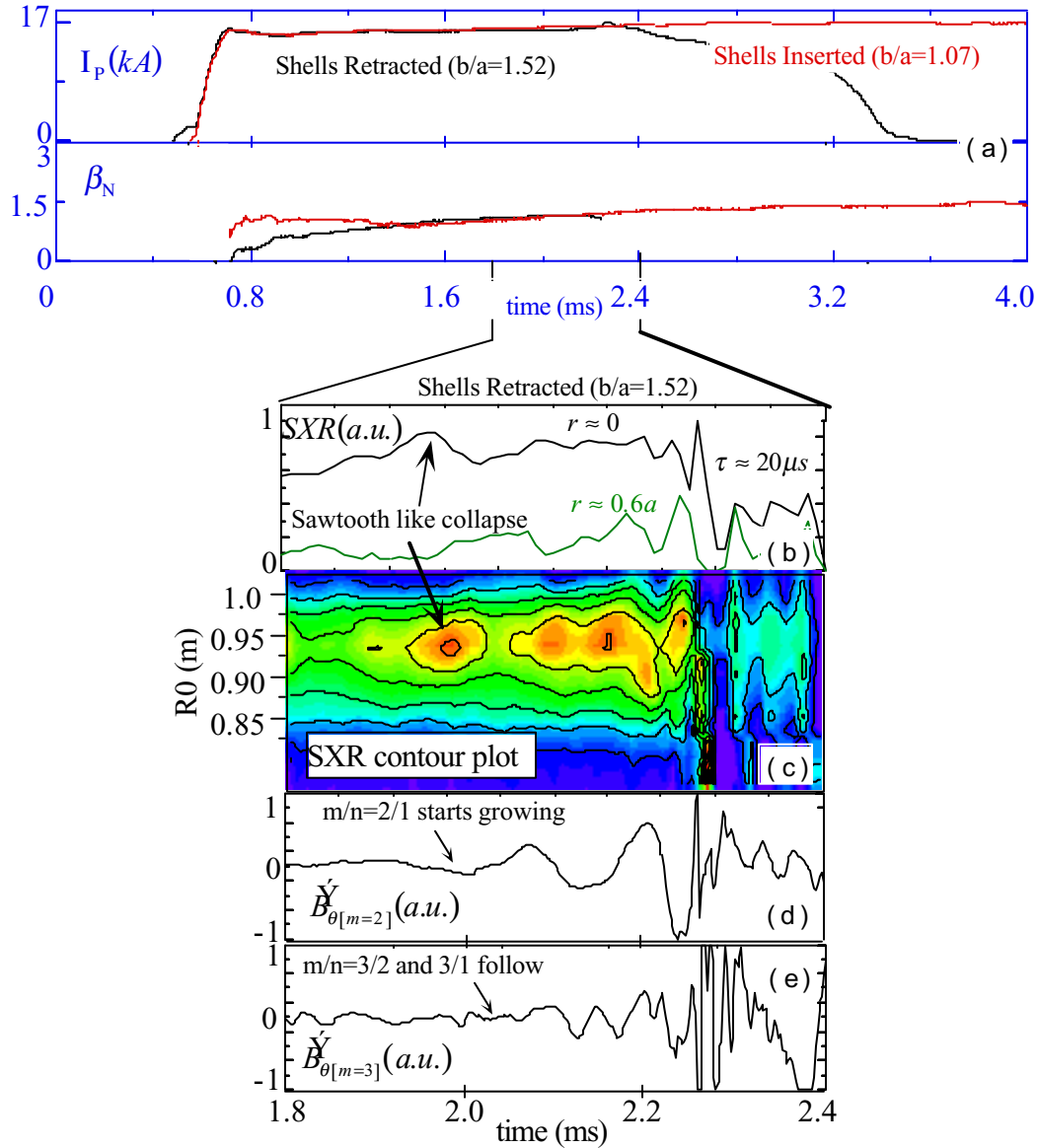
Fig 6.7 Disruption sequence for a rapid formation discharge with the shells retracted at high $\beta_N \approx 1.5$ showing (a) total plasma current and β_N (b) SXR signals from one cental channel and one edge channel (c) a SXR contour plot (d) m/n=2/1 (e) 3/2 and 3/1 magnetic perturbation

triggered the growth of magnetic perturbations. These fluctuations start with a structure of

m/n=2/1 and 3/2. Then immediately prior to the disruption, the magnetic detectors indicate a

growth of an m=3, n=1 perturbation and the soft x-ray contours suggest there is a strong

internal m=1 component of this global mode. All of this MHD activity leads to a very fast

($\tau \approx 20\mu s$) thermal crash as seen on the sxr central channel. Coincident with that crash, a

plasma current positive "spike" ($\delta I_\mathrm{P}/I_\mathrm{P} \approx 10\%$) arises on the total plasma current trace. These are the expected signatures of a disruptive instability as mentioned in chapter 3. It is important to point out that the harmonic content of the disruption pre-cursor mode is distinct from the low β current ramp case which was primarly an external m/n=3/1 pre-cursor mode. Hence the identification of this mode that grows with its different component at high β_N, having rational q=m/n surfaces both inside the plasma (2/1) and outside the plasma (3/1), as a global plasma mode that causes the termination of the discharge.

In Fig 6.8, the MHD and SXR activities of a comparable discharge formed with the shells fully inserted (b/a=1.07) are displayed. Again, raw data and a contour plot from the SXR diagnostic are shown along with the signals from the Fourier-analyzing Rogowski coils sensitive to m=2 and m=3 magnetic fluctuations. Also indicated is the time period of the disruption for the shells retracted case. The sequence of the disruptions begins similarly to the shells retracted case with the SXR central channel exhiniting sawtooth-like collapses, indicating periodic internal profile modifications. This leads again to MHD fluctuations developing and both the m=2 and m=3 components start to grow, however with reduced amplitudes and growth rates. The plasma continues to heat up as evident from the SXR contours and the MHD mode does not appear to affect the discharge. No disruption occurs as long as the current profile is kept sufficiently broad with a moderately positive current ramp.

In order to further illustrate how the disruptive mode gets contained when the shells are inserted, Fig 6.9 shows a comparison of the amplitudes of the 2/1 and the 3/1 components for both the shells inserted and shells retracted. The time period shown here
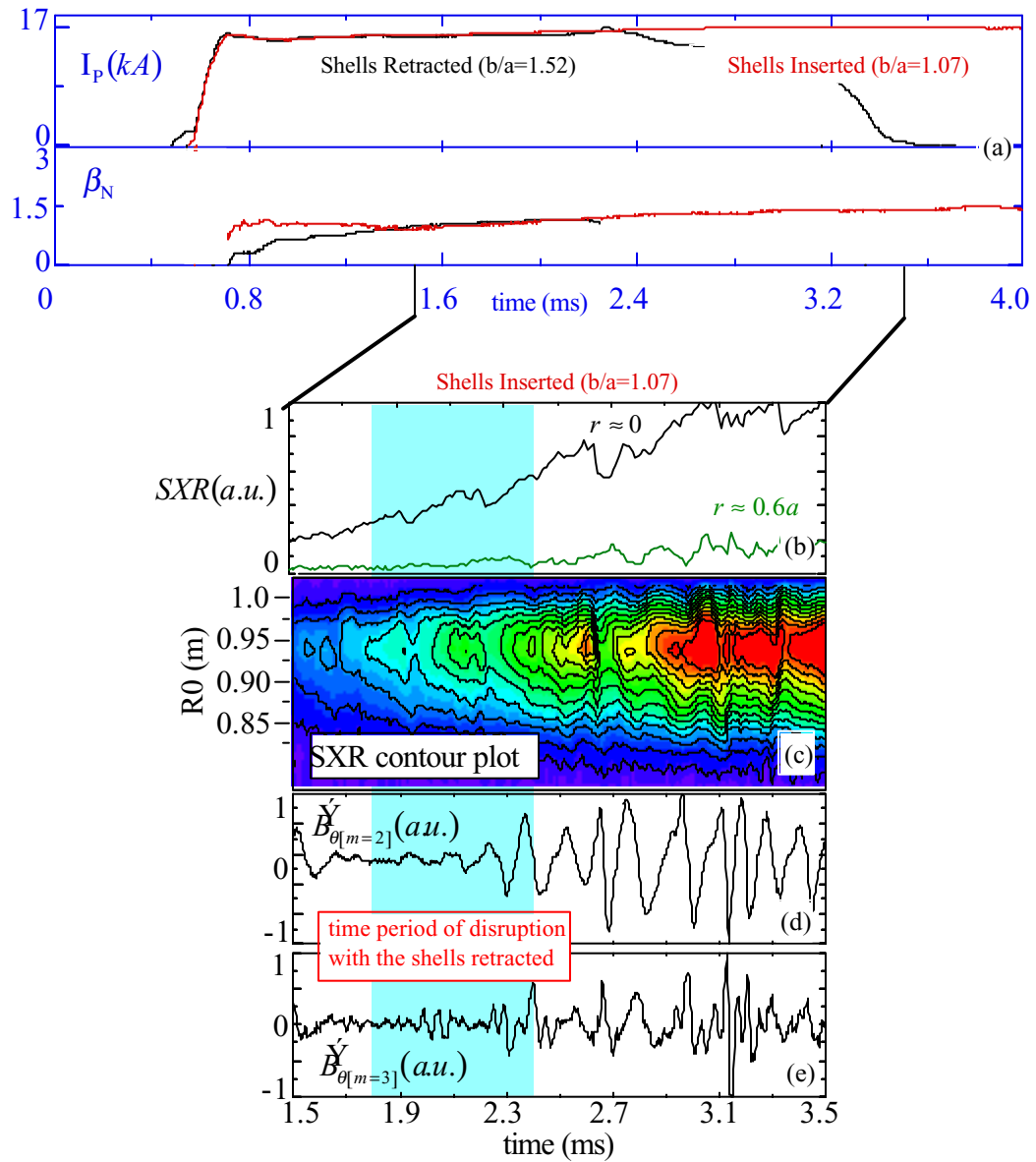
Fig 6.8 (a) Plasma formed with the shells inserted exceeds $\beta_N \approx 1.5$ (b)-(e) Internal fluctuations do not terminate the discharge

is that of the disruption for the shells retracted case. Shown overlayed in red is an average value of these amplitudes. It is evident from the plots that the 2/1 and 3/1 components of the disruptive mode are at least three times larger in amplitude in the case where the shells are

retracted than when the shells are inserted, again confirming the observation of shell satbilization of the pre-cursor mode for β-limiting disruptions.

(a) $\left.\left|\tilde{B}_{\theta\,[m=3,\,n=1]}\right|\right|_{r_{q=m/n=3/1}}$ (b) $\left.\left|\tilde{B}_{\theta\,[m=2,\,n=1]}\right|\right|_{r_{q=m/n=2/1}}$
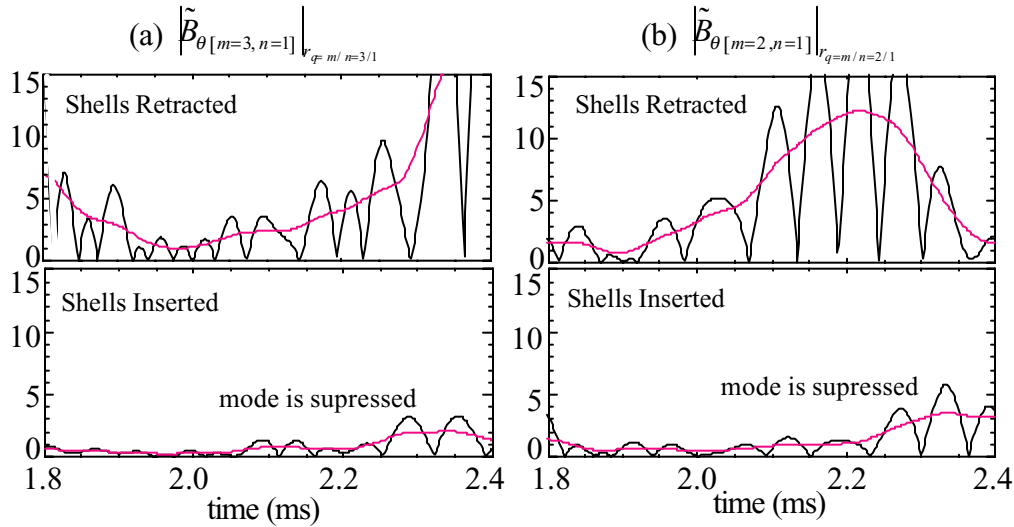
Fig 6.9 Mode amplitude comparison for discharges with the shells at b/a=1.52 and b/a=1.07 showing (a) the 3/1 component (b) the 2/1 component

6.4 Tearing modes in wall-stabilized discharges

Although the segmented conducting wall prevented large scale disruptive instabilities when it was close-fitted to the surface of the plasma, it did not completely eliminate disruptions on HBT-EP. In fact, wall stabilized discharges do end with a disruption that is due to slowly growing and satured rotating internal perturbations. Figure 6.10 shows the time evolution of the totat plasma current and position for a shell scan obtained for rapid formation discharges. The plasmas are similar except for the position of the conducting wall which was varied systematically in 2cm increments. With the shells retracted, the plasma disrupted as $\beta_N \approx 1.5$ and its disruption mechanism was examined earlier. One immediate observation is the orderly extension of the pulse length or plasma lifetime as the shells are moved closer to the plasma. The

improvement is at least by a factor two. Another observation from this plot, supported by larger data sets, is the indication that
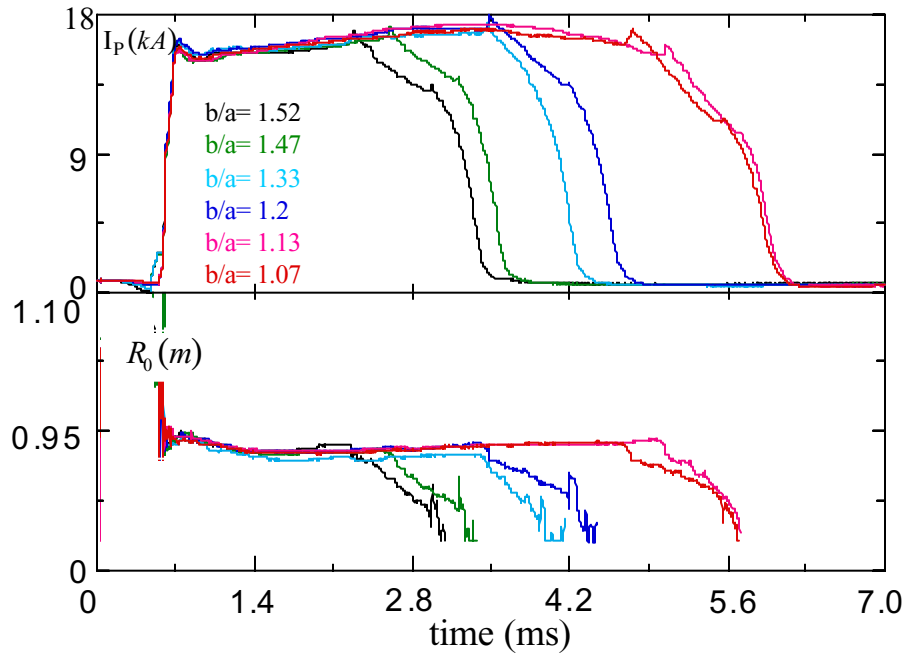

Fig 6.10 Shell scan showing total plasma current and positions as b/a=1.52 is incrementally changed to b/a=1.07.

disruptions are prevented if the shells are positioned such that b/a < 1.2 and a moderate current ramp of $dI_P/dt \approx 0.5\ MA/s$ is maintained. Finally, it is evident from the total plasma current traces that the wall-stabilized discharges disrupt during the current ramp-down phase of the discharge. Next, these internally caused disruptions are examined.

6.4.1 "Rapid formation" wall-stabilized discharges

In order to understand the disruptions observed in wall-stabilized discharges (that is discharges in which rapidly growing disruptive instabilities are suppressed by the close-fitting conducting wall), the plasma with b/a=1.07 plotted as part of the shell scan in Fig 6.10 is examined in some details at the end of its lifetime. Figure 6.11 the current-ramp down phase of

the discharge as well as the internal fluctuations as detected by the Mirnov coils and SXR
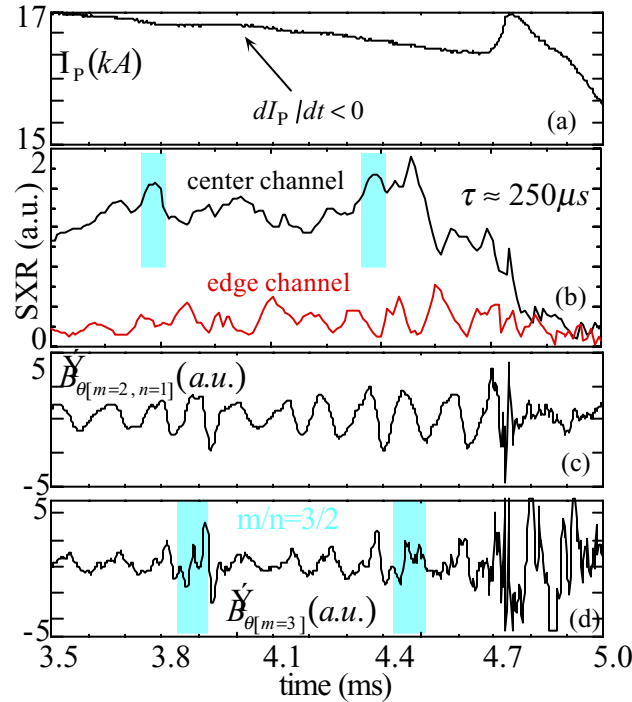
measurements.

**Fig 6.11 Disruption sequence for rapid-formation plasmas with b/a=1.07
Shown are (a) total current (b) 2 SXR channels (c) internal fluctuations
and (d) edge fluctuations**

At $t \approx 3.5ms$ the ramp down phase accompanied by sawtooth-like collapses (shaded

area on the plot) and instabilities with m/n=1/1, 2/1 and 3/1 components. The perturbations

rotate in the electron drift direction and generally possess the same frequency. Occasional bursts

of an m/n=3/2 perturbation immediately following sawtooth collapses are also seen at twice the

frequency of the n=1 components implying rigid toroidal rotation. At $t \approx 4.5ms$ a stronger than

before sawtooth crash occurs in the core of the plasma (SXR center channel) modifying the

internal profile of the discharge and causing its termination. The energy quench is gradual as

evident by the slow ($\tau \approx 250\mu s$) thermal collapse. It is that loss of heat from the center coupled

with the presence of the internal fluctuations

94

that brings about the termination of the discharge. Figure 6.12 shows the SXR signals from two diagnostics on HBT-EP, the 16-channel array and the Tomography system. The measurements show m=1 and m=2 internal fluctuations prior to the discharge disruption in the $dI_P/dt < 0$ phase. As a matter of fact, internal, current-gradient-driven tearing modes, with a strong m=2, n=1 component, have always been linked to disruptions in tokamaks.
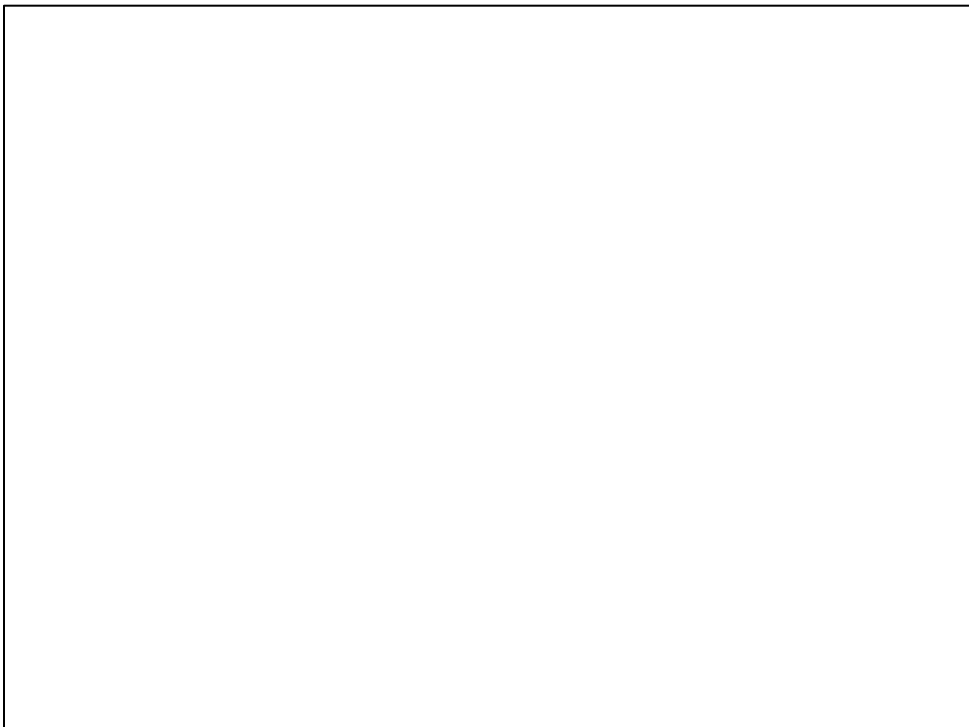
6.4.2 "Current-ramp" wall-stabilized discharges

Similarly to rapid formation plasmas, wall-stabilized current-ramp discharges also disrupt in their ramp down phase. Figure 6.13 displays the end period of the shells inserted discharge shown earlier. The current ramp down phase starts at $t \approx 4.4ms$, the plasma's

internal profile starts to dynamically change as evident from the sawtooth-like collapses seen on

the central SXR channel. This is accompanied all along by magnetic fluctuations with a strong

m/n=2/1 mode component having a rational q=m/n surface inside the plasma.
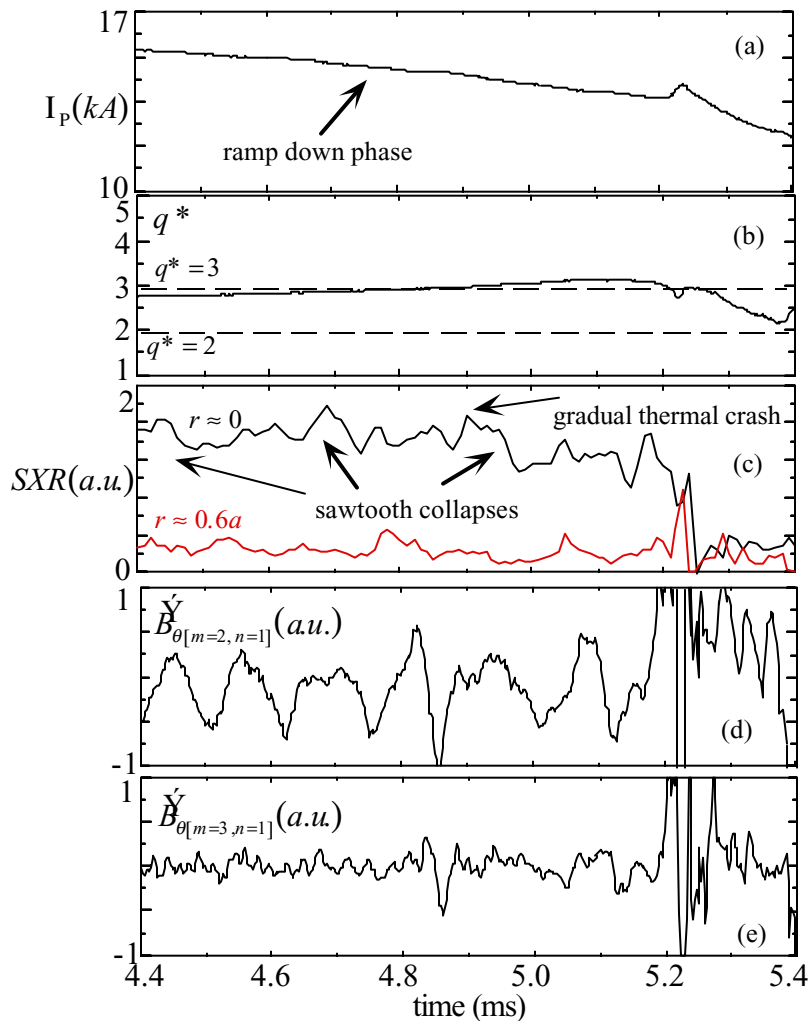
Fig 6.13 Disruption mechanism for a current-ramp wall-stabilized plasma shown are (a) total current (b) edge-q (c)-(e) internal fluctuations

At $t \approx 4.85ms$ edge-q goes above 3 indicating that the q=m/n=3/1 rational surface is

entering the plasma. This is followed by enhanced fluctuations on the m=3 magnetic perturbation

monitor. Shortly after, at $t \approx 4.90ms$, a strong sawtooth-like collapse also seen on the central

SXR channel triggers a gradual slow thermal decline, modifying the internal profile. This together with the 2/1 internal mode leads to the discharge termination at $t \approx 5.2 ms$.

6.5 Disruptions with b/a=1.52 vs disruptions with b/a=1.07

In order to gain more insight on the disruption mechanisms for both the shells retracted and shells inserted cases, the SXR emissivity profiles for rapid formation discharges formed with b/a=1.52 and b/a=1.07 are examined. For better correlation with the magnetic perturbations detected by the Mirnov coils, the fluctuating part of the SXR profiles are selected by simply substracting the equilibrium profile. Then, this fluctuating profile is decomposed into a symmetric or even part and a non-symmetric or odd part. The idea is that the even part will provide information on m=even (e.g. m=0,2) components of the disruptive mode and the odd part on m=odd (e.g. m=1,3) components. Figure 6.14 displays the results obtained for the odd decomposition and Fig 6.15 shows the results for the even decomposition.

**Fig 6.14 Odd-decomposed SXR profile fluctuations prior to disruption
for shells retracted (b/a=1.52) and shells inserted (b/a=1.07) cases**

The time periods are chosen similar to the ones in the previous sections starting with the appearence of MHD activity and finishing with the loss of the discharge for both wall positions cases.
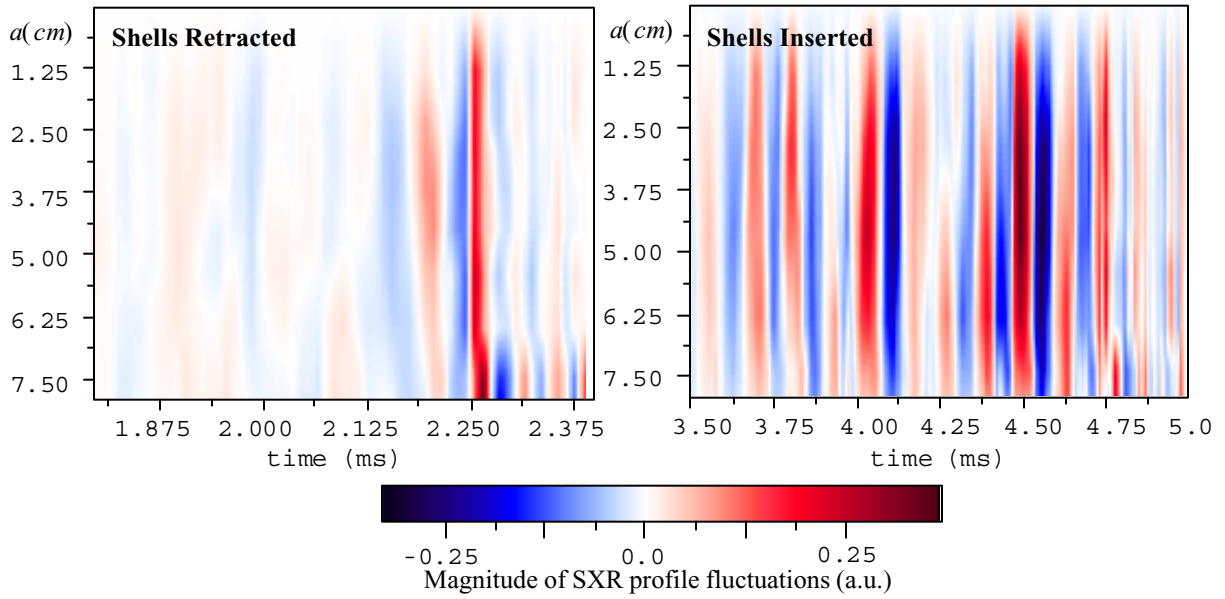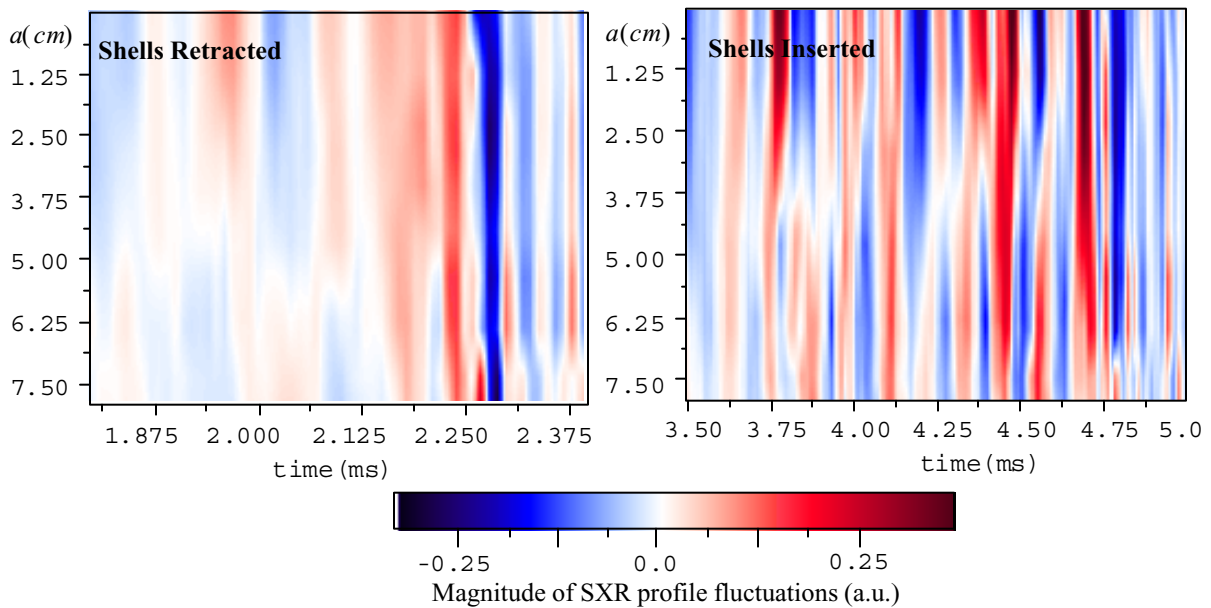

**Fig 6.15 Even-decomposed SXR profile fluctuations prior to disruption
for shells retracted (b/a=1.52) and shells inserted (b/a=1.07) cases**

98

The first observation is that the magnitude of both the even and odd fluctuations for the shells-inserted case prior to disruption is higher (at least by a factor of 2) than the one with the shells retracted prior to disruption. This suggests that the internal fluctuations are stronger in the shells inserted case, confirming the idea that the disruption with the shells inserted is an internally induced one. Looking more closely at each component, there are no significant odd fluctuations prior to the termination of the discharge for the shells retracted case except for the large m=1 type displacement immediately $(t \approx 30 \mu s$ before$)$ prior to the disruption. This, in contrast to the shells inserted case where repetitive odd fluctuations appear all along getting stronger coincidently with sawtooth collapses at $t \approx 4ms$ and $t \approx 4.5ms$ when the final gradual thermal loss begins to occur. The observations are slightly different for the even fluctuations. An m=even component begings to develop near the center for the shells retracted case at $t \approx 1.9ms$. Shortly after, the component grwos stonger and propagates to englobe the plasma all accross from center to edge. This coupling to the egde of the even fluctuations at $t \approx 2.15ms$ together with the growing of the external m/n=3/1 component as described earlier is the cause of the disruption, that manifests itself through the m=1 displacement, the rapid thermal crash and the positive total current spike. As for the even signal for the shells inserted case, the strong fluctuations near the core and all accross the plasma together with the odd fluctuations mentioned before and the periodic profile modifications from sawtooth collapses all indicate strong internal activity that lead to the termination of the discharge.

The point to remember is that when the shells are retracted, disruptions have an external (external to the plasma) character to them whether they are caused by external kinks (current-ramp discharges) or high β_N (rapid formation discharges). When the shells are close-fitted to

99

the surface of the plasma, the fast external disruptive modes are stabilized but the residual internal modes togther with internal profile changes cause the disruption which essentially has and internal character to it. Intuitively, it is not hard to think of resonant surfaces of modes exiting the plasma and if they encounter the wall (shells inserted) they are stabilized if not, the mode explodes and the plasma disrupts. Where as if the resonant surfaces of modes remain inside the plasma, the conducting walls, even near the surface of the plasma, can do very little to stabilize them, hence the inernal disruptions in these shells inserted discharges.

Chapter 7
DISCUSSION

7.1 Summary and discussion

One of the main objectives of the HBT-EP experiment is the investigation of passive stabilization of rapidly growing $\left(\tau \approx 10's \text{ of } \mu s \right)$ disruptive modes using a set of segmented conducting plates around the plasma.

The conducting wall studies concentrated on two classes of discharges. These were the "current-ramp" discharges that are susceptible to external kinks disruption precursors and the "rapid formation" discharges that disrupt at high β_N.

The segmented conducting wall was shown to suppress the growth of β-limiting instabilities in HBT-EP discharges. The disruptions caused by these pressure driven instabilities, with the shells retracted, started in the core of the plasma and then coupled to an external component, giving rise to a global mode displaying m=1, 2 and 3 magnetic fluctuations that terminated the discharge. When the shells were close-fitted to the surface of the plasma, the growth of the m=2 and m=3 components of the mode decreased, disruptions were eliminated and the discharge lifetime was extended.

The segmented conducting wall also suppressed the external kinks associated with current-ramp discharges. These rapidly developing modes with growth times on the order of tens of microseconds had a strong m/n=3/1 exploding external component; they appeared in conjunction with shells retracted discharges and caused their termination. They were stabilized as the shells were placed near the surface of the plasma.

101

While the lifetime of wall-stabilized discharges was extended and their fast growing dangerous disruptive modes were eliminated, these plasmas did eventually disrupt in their ramp-down phase as the total current decayed. The disruptions were caused by internal modes (modes with rational surfaces inside the plasma) that developed on a slow time scale on the order of tens of milliseconds and appeared to be tearing like. They were observed in both classes of discharges.

The disruptions examined corresponded to three types of current profiles that can be obtained on HBT-EP. These are associated with different current ramp rates and ramp periods in the discharge's lifetime. A simulation was done to model these current profiles and study their modification as they relate to disruptions and plasma-wall separation.

Disruption sequences were compared for both shell positions. In the case of the shells retracted, the disruptive events were external to the plasma or near its edge. In the shells inserted case, the precursors that caused the disruptions were all internal from within the core of the plasma. The differences and similarities in the characteristics of the three representative

	b/a=1.52 *High edge current*	b/a=1.52 *High plasma pressure*	b/a=1.07 *Wall-stabilized*
dI_P/dt	Positive (>0)	Positive (>0)	Negative (<0)
Loop voltage	Negative spike	Negative spike	Negative spike
Current Ip	No current spike Ip deterioration followed by loss of current channel	Current spike $\delta I_P/I_P \approx 10\%$ Current quench phase followed by loss of current channel	Current spike $\delta I_P/I_P \approx 10\%$ Current quench phase followed by loss of current channel
Thermal collapse	—	$\tau_{crash} \approx 20\,\mu s$	$\tau_{crash} \approx 200\,\mu s$
Precursor instability	External kink mode	Global kink mode	Tearing mode
Mode numbers (m/n)	Strong edge 3/1	coupling between 2/1, 3/1 and 1/1	Strong 2/1 with bursts of 3/2
β_N	<1	~1.5	~1.9
Disruption sequence	1)Edge-q drops below 3 2) Mode amplitude explodes 3) Discharge disrupts	1) Sawtooth collapse in the center 2) MHD modes start to grow (2/1 and 3/1) 3) Thermal crash 4) Current quench and disruption	1) Repetitive sawteeth collapses 2) Internal modes (2/1) are present with a constant amplitude 3) Gradual thermal decline 4) Current quench and disruption

Table VII.1 Comparison of disruption features for plasmas with shells inserted and shells retracted

disruptions were outlined. They are summarized in table VII. 1 below.

The occurrence of disruptions in wall-stabilized (shells fully inserted) discharges, accompanied by slowly growing internal precursors, points to the necessity of providing active control to these internal instabilities which were identified as tearing modes with a strong

m/n=2/1 component. Tearing modes grow on a resistive diffusion time scale (one thousand times slower than ideal kinks) making dynamic stabilization feasible. Saddle-shaped coils mounted around the torus can be used to generate localized magnetic perturbations which can influence the instability's amplitude and frequency.

The feedback approach planned for HBT-EP utilizes the application of oscillating magnetic perturbations for mode rotation control and closed loop synchronous feedback for mode suppression. Both will be done using high-power amplifiers and a set of modular saddle coils.